Alma Mater Studiorum · University of Bologna

School of Science
Department of Physics and Astronomy
Master Degree in Physics

Development of imaging techniques for scintillation light tracks in a novel neutron detector

Supervisor:
Prof. Cristian Massimi

Submitted by:
Samuele Lanzi

Co-supervisor:
Prof. Francesco Giacomini

Academic Year 2023/2024

ABSTRACT

Track imaging systems have been employed in nuclear, particle, and astroparticle physics to reconstruct particle interaction topologies. Early methods relied on bubble chambers and manual analysis, but modern techniques use advanced silicon detectors and scintillators to convert radiation into visible light. Sensitive photodetectors, such as SiPM matrices and CMOS cameras, capture this light, converting it into a digital signal, which is then processed to form an image. Coupled with sophisticated computational algorithms, these systems extract physical information from the images, eliminating the need for manual analysis. This work presents RIPTIDE, an innovative recoil-proton track imaging system designed for fast neutron detection, using the images generated from the detected light. RIPTIDE employs neutron-proton (n-p) elastic scattering in a plastic scintillator to produce scintillation light, which is captured in images to reconstruct scattering events in space and time. The primary objective is to develop novel track reconstruction techniques to determine the energy of incident neutrons using two orthogonal projections of the scintillator on the sensor. A hybrid approach combines the Hough transform with statistical moment-based methods to determine track direction and orientation, while deep-learning techniques are employed to remove optical aberrations from the tracks. This improves the accuracy of track length reconstruction. From the corrected images, proton energies are calculated, enabling the reconstruction of full neutron kinematics. Promising results are shown, highlighting the successful neutron energy reconstruction from both single and double scattering events.

Contents

List of Figures

Introduction

Innovation in neutron detection plays a critical role in many scientific and practical applications, including fundamental physics, medical diagnostics and environmental monitoring. Fast neutrons, in particular, pose a unique detection challenge due to their lack of electrical charge, which limits direct interaction with matter. This challenge has led to the development of increasingly sophisticated detection systems, driven by advances in both material science and computational advances.

This thesis introduces RIPTIDE (RecoIl Proton Track Imaging DEtector), an innovative detection system concept designed for fast neutron tracking. RIPTIDE is aimed at imaging the scintillation light generated when neutrons elastically scatter off protons in a plastic scintillator. By reconstructing the proton recoil tracks using stereoscopic imaging, the system can determine both the energy and the trajectory of the incident neutrons. A key objective of this work is to develop novel techniques for track reconstruction and energy estimation, using two orthogonal projections of proton tracks, enhanced by advanced image processing and deep learning methods.

The structure of this thesis is as follows:

- **Chapter 1** outlines the scientific motivations for neutron detection and explores several key applications, such as space radiation protection, hadrontherapy, and solar neutron studies. The chapter also reviews the state of the art in neutron detection technologies, with a particular focus on recoil proton imaging techniques.

- **Chapter 2** introduces the concept and working principle of RIPTIDE, based on neutron-proton elastic scattering. It discusses the detector's design, the materials used, and the Monte Carlo simulations performed to validate the detection concept. This chapter also provides a detailed description of the components of the detector, including the scintillator, optical systems, and electronics.

- **Chapter 3** describes the imaging reconstruction techniques used to analyze the proton tracks. It presents methods for determining the direction and orientation of the tracks, such as the Hough transform, and explains how deep learning is applied to correct optical aberrations and accurately estimate the proton track length.

- **Chapter 4** focuses on estimating neutron energy and momentum from single and double scattering events. It describes the reconstruction of proton energy and the calculation of neutron kinematics, using both experimental data and simulation results to demonstrate the the system's efficacy.

Through the development of RIPTIDE, this work demonstrates how a combination of classical algorithms and deep learning techniques can enhance the precision and reliability of fast neutron tracking, paving the way for advancements in both scientific research and practical applications.

1 The critical role of neutron tracking

Neutron detection systems are essential tools for both fundamental and applied research. As neutrons do not directly ionize matter, their detection relies on neutron-nucleus interactions producing detectable charged particles or electromagnetic radiation. Neutrons are categorized based on their energy, as illustrated in Figure 1.1. This work specifically focuses on the detection of fast neutrons. This chapter explores the motivations behind neutron detection and the current state-of-the-art techniques for fast neutron detection based on recoil proton detection.

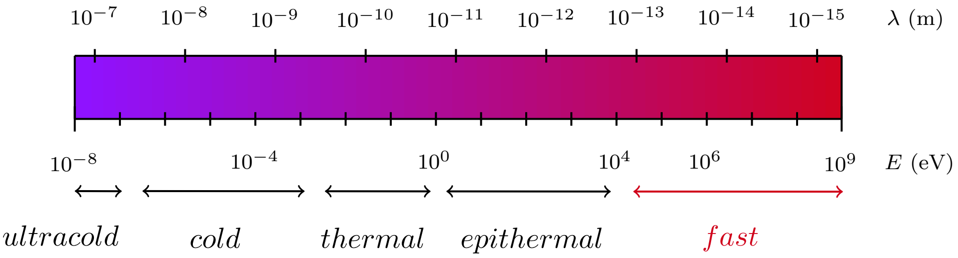

FIGURE 1.1: *Neutron classification based on kinetic energy and the corresponding de Broglie wavelengths is reported.*

1.1 Scientific motivations

This section shows the relevance of neutron detector applications in different research fields; for instance, astrophysics, space radioprotection, nuclear medicine, nuclear physics, and agriculture.

1.1.1 Solar neutrons

The Sun, unlike most other celestial objects, emits neutrons that can be detected near Earth. During times of high solar activity, and especially during intense solar flares, particles are accelerated to very high energies. These high-energy particles interact with the solar atmosphere, creating high-energy neutrons. Some of these neutrons escape the Sun and can be detected on Earth with energy that ranges in 10-50 MeV, helping scientists study the acceleration processes in solar flares. By analyzing the detected neutron flux, researchers can learn about the acceleration timescale and the total number of particles accelerated. Unlike charged particles that get bent by the Sun magnetic field, neutrons, which have no electrical charge, travel in a straight line from their source directly towards Earth (Figure 1.2) [8]. However, it is important to consider the neutron mean lifetime, which is 14.63 min. Therefore, during this transit from the Sun to the Earth, a substantial portion of these neutrons undergoes beta decay; as a result, only about 30% of the initially emitted neutrons manages to reach Earth vicinity.

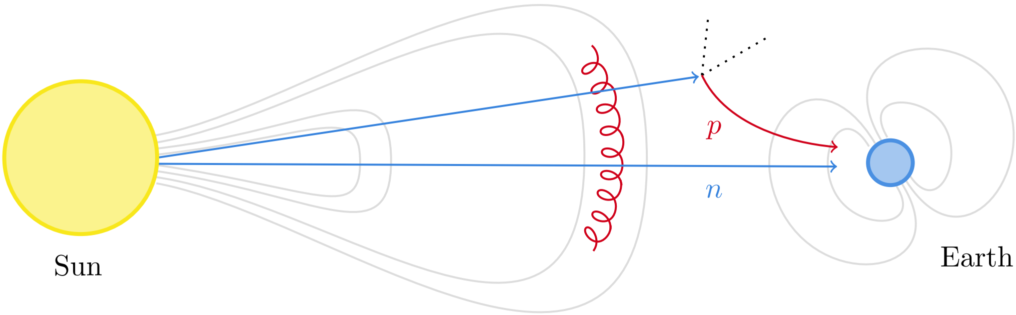

FIGURE 1.2: *General view of interplanetary space during a solar flare. Protons are trapped in the magnetic field. Neutrons can reach Earth, but some decay into protons along the way.*

In Table 1.1 examples of the neutron time of flight for different neutron kinetic energies is reported. Ground-based facilities can continuously monitor space radiation for solar neutrons, but the Earth atmosphere reduces the neutron flux significantly. To address this issue, measurements are best taken at high-altitude observatories or on spacecraft. Clearly, a neutron detector with track-reconstruction capability is essential to determine if detected neutrons come from the Sun or are originated by cosmic-ray interaction in the environment.

Energy (MeV)	TOF (minutes)	Number of $T_{1/2}$
1000	9.50	0.93
500	11.0	1.1
100	19	1.9
10	57	5.6
1	180	17
0.1	560	56

Table 1.1: *Neutron time of flight from the Sun to the Earth surface and comparison with neutron half life.*

1.1.2 Space radioprotection

Radiation exposure during space exploration is a major threat to astronaut health, causing risks like cancer, tissue damage, nervous system issues, and acute radiation sickness. Space radiation, consisting of high-energy protons and heavy nuclei, is by far more dangerous than radiation on Earth and creates uncertainty in predicting health risks and evaluating protective measures. While there exist guidelines for crew exposure and spacecraft design for short missions in low Earth orbit, we lack enough information for long-duration missions. A well-known example is a trip to Mars, where astronauts would face a much harsher radiation threat.

Unlike Earth, Mars lacks a global magnetic field, leaving it exposed to a constant barrage of galactic cosmic rays and solar energetic particles bursts. Data from Curiosity rover [12] shown in Figure 1.3 suggests the Martian surface receives an average dose of 0.67 mSv per day, while astronauts traveling in a spacecraft for 180 days each way could be exposed to 1.8 mSv daily. Combining surface stay and travel, a total mission dose of 1 Sv is estimated, which increases the risk of fatal cancer by 5%. This exceeds NASA current limit for low Earth orbit but falls within limits set by some other space agencies. Recognizing the knowledge gap, NASA is working with the National Academies Institute of Medicine to define safe radiation exposure limits specifically for deep space missions like a trip to Mars.

A significant gap is the lack of experimental data on how neutrons and light ions are produced in thick shielding by galactic cosmic rays. Neutrons, which have a long range and high biological impact, are particularly dangerous. They are easily produced during nuclear fragmentation and, because of their abundance and low interaction rate, pose a challenge for passive shielding design. This issue is especially important when designing planetary habitats. Current particle transport codes used in space radiation research show large discrepancies in predicting neutron and light ion production in thick shields. These discrepancies are due to limited data on scattering at large angles and uncertainties in nuclear physics models describing the breakup and de-excitation of projectiles and targets [18]. In this research field, the availability of a neutron tracker would make it possible to collect the missing experimental data.

Figure 1.3: *Rover Curiosity on Mars' surface (Credits: NASA/JPL-Caltech/LANL).*

1.1.3 Hadrontherapy

In radiotherapy for cancer treatment, radiation is used to inhibit cancer cell reproduction. However, in conventional radiotherapy with γ-rays, significant portions of the patient body are exposed, potentially causing secondary radio-induced tumors. Current research focuses on targeting cancer cells while minimizing radiation exposure to healthy tissues. Hadrontherapy is a cancer treatment using fully ionized ions, such as protons and carbon ions, which release most of their energy at the end of their path, thus localizing radiation to the cancer region. This technique, with particle energies between 200 and 400 MeV, is ideal for treating deep-seated tumors or tumors near organs at risk.

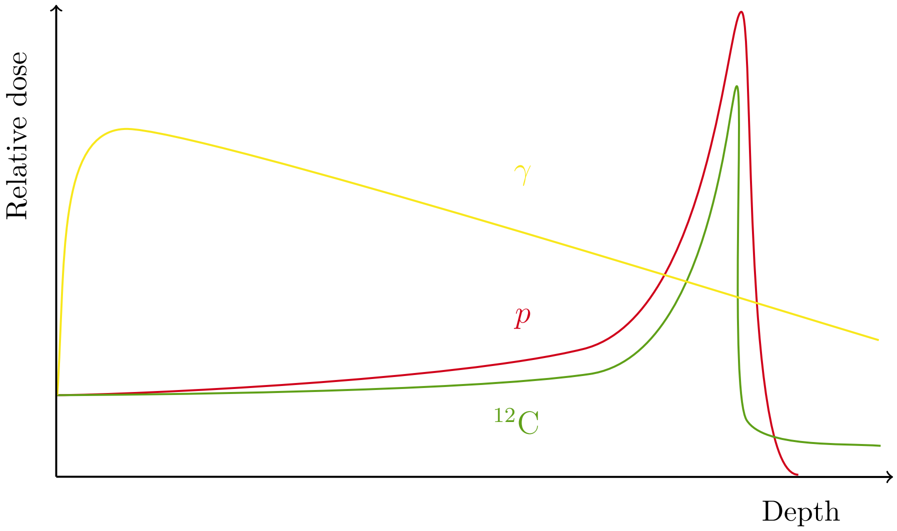

FIGURE 1.4: *Depth-dose profiles of photons (yellow line), protons (red line) and carbon ions (green line) in water. Differently than photons, whose dose deposition is higher at skin surface, ions release the most part of the dose at the end of the path. However, in the graph it is possible to see a tail beyond the carbon ion peak. It is due to projectile fragmentation.*

The concept behind hadron therapy involves taking advantage of the specific behavior of heavily charged particles interacting with matter (known as the Bragg curve) to concentrate the dose of radiation in cancerous tissue while minimizing exposure to healthy tissue. The key point to note from Figure 1.4 is that the majority of the dose is delivered to the patient at the end of the particle path, while the tissue before and after the peak is protected from excessive radiation exposure. In contrast, when considering photon interaction with matter, the highest dose is deposited at the skin entrance, followed by a rapid decrease. In conventional radiotherapy for deep tumor masses, a significant amount of radiation is absorbed by healthy tissues. In hadrontherapy, in addition to the dominant Coulomb collisions, nuclear interactions play a significant role. These interactions can be categorized as either elastic or inelastic. Elastic interactions alter the direction and energy of the primary particles, while inelastic interactions fragment the primary particles into smaller components. The high energies employed in hadrontherapy can break nuclei into protons, neutrons, and various fragments, but they do not lead to further fractionation of nucleons. This phenomenon primarily affects nuclei with $A > 1$, such as carbon and oxygen present in human tissues. Unlike heavier ions, protons do not experience projectile fragmentation; in contrast, heavier ions, such as carbon, are susceptible to this phenomenon. As illustrated in Figure 1.4, fragmentation of either the target or projectile can lead to a dose release beyond the Bragg peak. This occurs because the fragments continue with velocities and directions that are similar to those of the primary particles. Determining the exact number and types of fragments produced is complex and can vary based on specific conditions, including the characteristics of the proton beam and the type of tissue being irradiated. Experimental initiatives, such as the FOOT [2] experiment, aim to accurately measure these cross-sections to enhance our understanding and predict the outcomes of proton beam interactions with human tissues. Such measurements are essential for optimizing treatment planning in hadrontherapy, ensuring both the safety and efficacy of the treatment.

To ensure accurate positioning of the Bragg peak within the cancer region during hadron therapy, even minor displacements due to patient movements must be accounted to improve precision. Therefore, irradiation machines need online control systems to verify the beam position in real-time. One proposed method is using a Positron Emission Tomography (PET) system. Radioactive nuclei produced during nuclear fragmentation, such as ^{10}C, ^{11}C, and ^{15}O, decay and emit positrons that annihilate with electrons, producing detectable photons. This allows the PET system to estimate the beam position. Additionally, we already know that common products of nuclear fragmentation are neutrons. Therefore, a device able to detect them and retrieve their origin in real-time could be considered as an alternative or concurrent device for the monitoring of beam position.

1.1.4 Measurement of the neutron-neutron scattering length

The neutron time-of-flight facility n_TOF [10] at CERN was developed to study neutron-nucleus interactions. It is able to work with a remarkably large span of neutron kinetic energies: from a few MeV to several GeV (Figure 1.5). Neutron cross-section measurements are performed exploiting the time-of-flight method. At the n_TOF facility, a pulsed neutron beam is generated via proton-induced spallation on a massive lead target. Initially-fast neutrons are moderated by a water slab in order to obtain the wide energy spectrum mentioned above. Neutrons are collimated towards two experimental areas, respectively positioned at 18.5 m (EAR2) and 185 m (EAR1) from the spallation target.

Recently, a proposal for the measurement of neutron-neutron scattering length was submitted [17]. The idea is to exploit the interaction of the two neutrons in the final

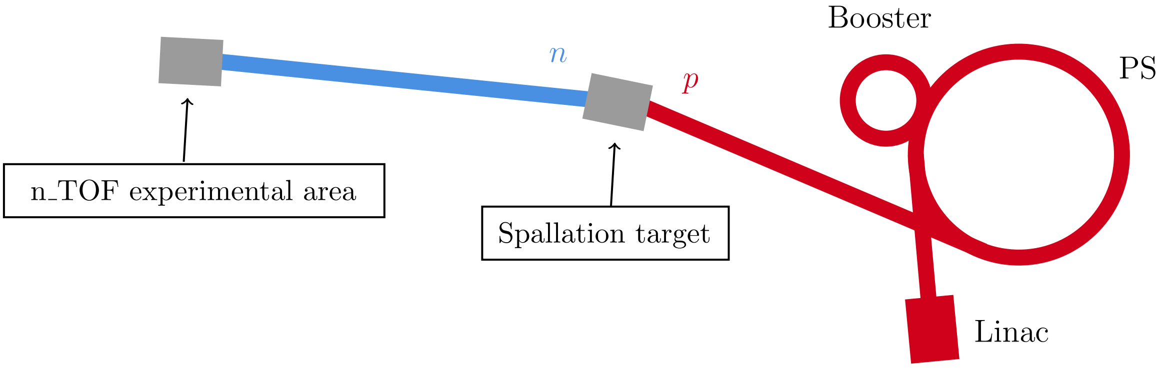

FIGURE 1.5: *Sketch of the n_TOF facility at CERN.*

state of the neutron-induced deuteron breakup reaction:

$$n +^2 \mathrm{H} \rightarrow p + n + n, \tag{1.1.1}$$

for determining the neutron-neutron scattering length in a wide energy range (namely between 10 and 100 MeV) in a single experiment. By taking advantage of the unique features of the updated n_TOF facility, the measurement can be carried out at EAR2. The experiment is based on the detection of the three outgoing particles in kinematic coincidence, leading to a full three-body kinematic reconstruction. The feasibility of this challenging experiment requires a preliminary experimental activity to investigate the possibility of using an active target based on a liquid scintillation detector highly enriched in deuterium, alongside the availability of a neutron tracker like RIPTIDE.

1.1.5 Agricultural applications

Soil moisture plays a critical role in regulating Earth water and energy cycles. It sustains plant life, influences weather patterns, and impacts runoff. Understanding soil moisture is crucial, and the neutron method offers a valuable tool [25].

Cosmic rays are a natural source of radiation on Earth. These highly energetic particles collide with the nuclei of atmospheric gases, producing showers of sub-atomic particles that are directed towards the soil surface. Along this path the newly accelerated particles continue to impact additional atmospheric nuclei causing further reactions as they travel. Over time the energy contained in the cosmic ray shower is dispersed among these numerous atmospheric collisions. This process gives rise to a measurable flux of fast neutrons near the Earth surface. These neutrons scatter isotropically and are slowed down mainly through collisions with hydrogen atoms in the environment. Once slowed by hydrogen collisions, they are absorbed by various soil and air elements. Because hydrogen has a much greater capacity than other elements to slow fast neutrons to the point of absorption, the presence of hydrogen on the surface and in the atmosphere is the primary means of fast neutron "removal" from any terrestrial system (Figure 1.6). Additionally, the main form of hydrogen in any terrestrial system is in the form of soil water molecules. As such, a relationship can be formed between counts of neutrons and the amount of water in a given area. Clearly, this techniques can benefit from the availability of a neutron detector sensitive to neutron direction.

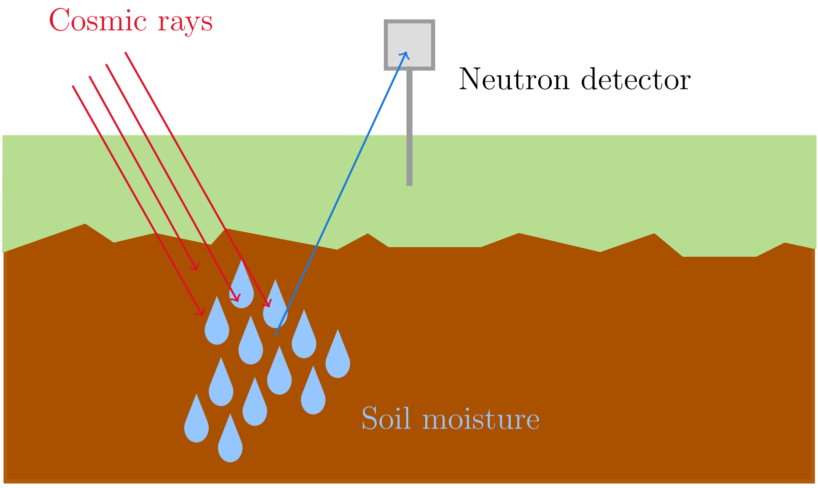

Figure 1.6: *Evaluation of soil moisture using a neutron detector.*

1.2 State of the art

The late discovery of the neutron in 1932 by Chadwick [6], thirteen years after the proton, highlights the challenges associated with detecting these particles. This section explores potential interaction mechanisms for neutron detection, followed by a detailed examination of novel techniques based on proton recoil. Finally, a short review of the current state-of-the-art in this detector category is presented.

1.2.1 Neutron detection mechanisms

The general principle of neutron detection involves a two-step process: initially, the neutron interacts with the detector material to produce charged particles. Subsequently, the detector generates an output signal based on the energy deposited by these charged particles. Here the focus is on charged particles, therefore, the first step is to identify possible charged particles resulting from neutron interaction mechanisms:

- **Absorption reactions with prompt emission**: Low-energy neutrons are typically detected indirectly through absorption reactions in materials with high neutron absorption cross sections, such as $^{3}\mathrm{He}(n,p)^{3}\mathrm{H}$, $^{6}\mathrm{Li}(n,t)^{4}\mathrm{He}$, $^{10}\mathrm{B}(n,\alpha)^{7}\mathrm{Li}$, and $^{235}\mathrm{U}(n,f)$. These materials undergo reactions that emit high-energy ionized particles, which create detectable ionization tracks.

- **Elastic scattering reactions**: High-energy neutrons are typically detected indirectly through elastic scattering reactions. Neutrons collide with nuclei in the detector material, transferring energy and creating ions that recoil, and are subsequently detected. Optimal energy transfer occurs when the mass of the target nucleus is comparable to the neutron mass, making hydrogenous materials (e.g., plastic scintillators or organic liquids) preferable for such detectors.

- **Inelastic scattering reactions**: very high-energy neutrons can also interact inelastically producing nuclear fragmentation causing the nucleus to break into two or more smaller fragments. This type of reaction can occur when the neutron has enough energy disrupting its internal structure. From this process, a multitude of charged particles can be produced.

By employing these interaction mechanisms, various neutron energy ranges can be effectively analyzed, providing comprehensive neutron detection capabilities for a wide range of applications.

1.2.2 Types of neutron detectors

In Section 1.2.1, we mentioned that neutron detection follows two steps. First, the neutron interacts with a material to produce charged particles that are detectable by the detector. These charged particles can then be observed using various types of detectors. Furthermore, fast charged-particle detectors can function as spectrometers (i.e., to measure the neutron kinetic energy) when combined with the Time-of-Flight technique.

We will now explore examples relevant to fast neutron detection, as this is the energy range of interest for fast neutrons:

- **Gaseous detectors**: An example is the fission chamber, a gas detector filled with a ^{238}U sample. In these detectors, neutron-induced fission produces charged fission fragments. The detector then functions as an ionization chamber, detecting the presence of neutrons by capturing these charged particles.

- **Semiconductor detectors**: An example is silicon, often used in combination with appropriate converters like ^{10}B or ^{6}Li. Another promising material is the diamond detector, which offers the advantage of being composed of carbon, resulting in a response similar to that of human tissue.

- **Scintillator detectors**: These detectors exploit the ability of certain materials to emit optical photons when excited by ionizing radiation. Neutron detection with these materials is possible due to the presence of nuclei that have a high cross section for neutron-induced reactions. In plastic scintillators, this mechanism is enhanced by the high proton density in hydrocarbons.

- **Passive detectors**: An example is photographic emulsion. In these systems, the presence of neutrons is indicated by the track of a recoil proton or other reaction products within the emulsion. The main drawback of this system is the complexity of the scanning process.

1.2.3 Recoil proton track imaging techniques

In recent years, a new method for detecting neutrons, known as Recoil Proton Track Imaging (RPTI), has received significant attention. This method aims to obtain information on neutron energy and direction by analyzing the scintillating light produced by proton tracks. This innovative detection technique needs two necessary elements: a neutron-to-proton recoil converter and a proton track imaging system. The former is needed to induce n-p elastic scattering and makes use of materials rich in protons (e.g. plastic); the latter is generally made of a scintillating material coupled to a real-time imaging device. The scattering needs to be elastic because the RPTI technique requires momentum and energy conservation. If the neutron source position is known, this technique can determine the neutron energy by observing a single neutron-proton scattering event. Considering the Figure 1.7, by applying the conservation of momentum and energy, and approximating the mass of the proton as equal to the mass of the neutron, we

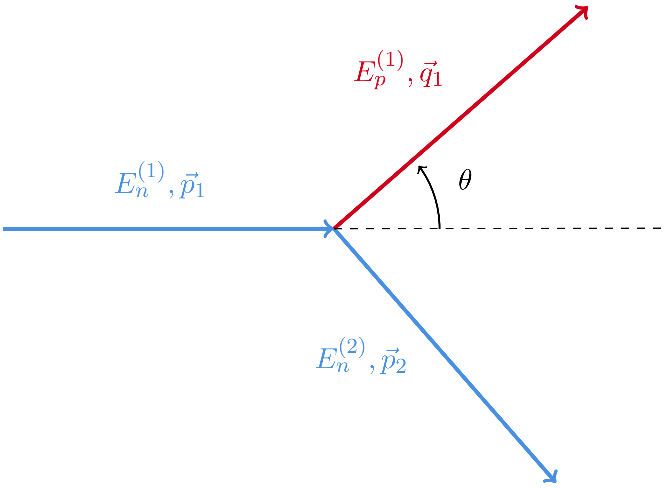

FIGURE 1.7: *Single scattering n-p.*

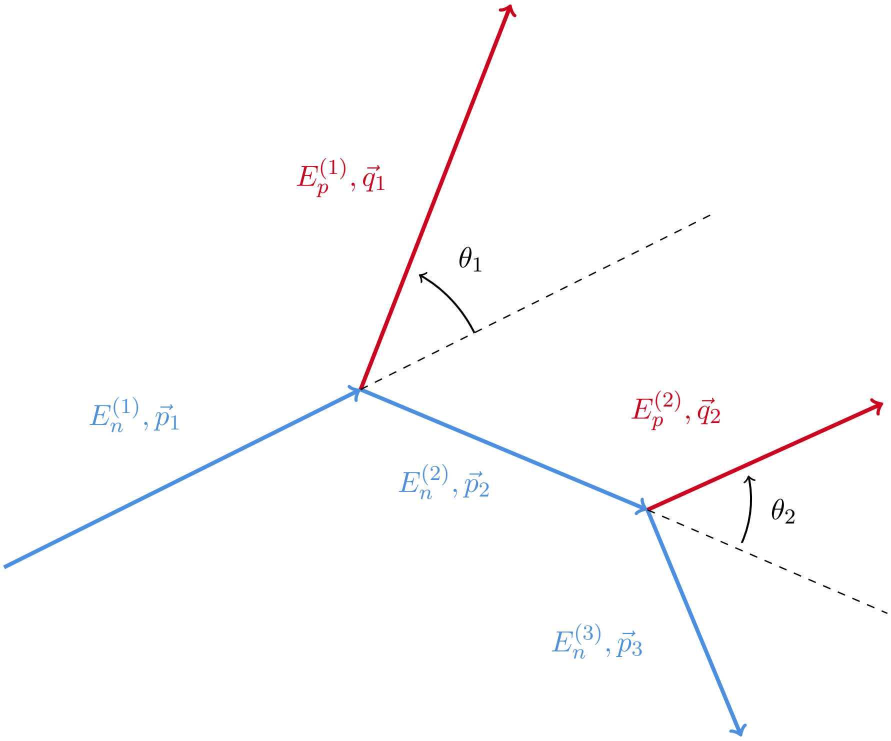

FIGURE 1.8: *Double scattering n-p.*

obtain:

$$|\vec{p}_1| = \frac{|\vec{q}_1|}{\cos\theta} \Leftrightarrow E_n^{(1)} = \frac{E_p^{(1)}}{\cos^2\theta}, \tag{1.2.1}$$

where E_n and E_p are the neutron energy before/after scattering and the proton energy after scattering, respectively. Given the approximation of the proton mass being equal to the neutron mass, the angle $\vec{q}_1$ and $\vec{p}_2$ is 90°. The proton energy E_p is obtained by measuring the length of proton track, known as *range*. The range R of a heavy charged particle in matter is related to its energy E via the formula:

$$R(E) = \alpha E^p, \tag{1.2.2}$$

where α depends on the material, p on proton energy. If the neutron interacts twice with protons, in what is called double scattering (Figure 1.8), we can fully determine the neutron energy and direction: by connecting the two interaction vertices, we can estimate the value of θ_2; then, using Equation 1.2.1 twice, we can reconstruct the full kinematics.

1.2.4 Solar neutron tracking detector (SONTRAC)

SOlar Neutron TRACking has been designed to operate in the energy region between 20 and 150 MeV, that is the energy range of neutrons produced in solar flares. It is based on non-relativistic double elastic scattering of neutrons with the protons in a plastic scintillator. Its hearth is based on a bundle composed of mutually perpendicular, alternating layers of parallel scintillating plastic fibers with a pitch of 300 μm, so that, when a sufficiently energetic neutron interacts with a proton inside the detector, the recoil proton is emitted with enough energy to travel several fibers before being stopped. The apparatus measures $5 \times 5 \times 5$ cm^3 and can display a grid of 150×150 pixels on each side. The fiber bundle is seen by two orthogonal photomultiplier tubes and by two orthogonal optics chains that include image tapers, image intensifiers and CCD cameras.

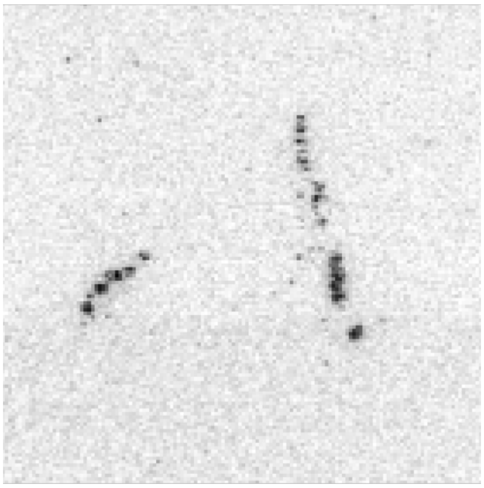

Figure 1.9: *Raw CCD image of a double scattering of a 65 MeV incident neutron obtained by SONTRAC [21].*

These two cameras provide a stereoscopic view of proton tracks. From the detection of double scattering, it is possible to reconstruct initial neutron energy and direction. In SONTRAC, energy and angular resolution of recoil protons have been determined to be $\delta E/E = 4.8\%$ and $\delta\theta = 4.6°$ at 35 MeV and they improve with energy [3]. It is worth to mention that SONTRAC obtained a 2D image of a n-p double scattering presented in an article in 1999 [21] (Figure 1.9), proving the practical possibility to detect this phenomenon.

1.2.5 Monitor for neutron dose in hadrontherapy (MONDO)

MOnitor for Neutron Dose in hadrOntherapy [24] has been designed with a configuration similar to SONTRAC. Again, a matrix of scintillating fibers constitutes the place of neutorn scattering and detection. The photons emitted by the scintillator are captured by an optical system. Unlike SONTRAC, this detector has been designed to detect neutrons produced during particle therapy treatments, whose energies range between 20 and 600 MeV. The optical sensors used in MONDO consist of a signal amplifier based on a gas electron multiplier, and an acquisition system based on a CMOS Single Photon Avalanche Diod (SPAD). In 2018, a first simple prototype of the MONDO project, Penelope, was developed and its output results were compared with a Monte Carlo simulation. Penelope was made of a $4 \times 4 \times 4.8$ cm^3 cube of scintillating fibers and was tested for the detection of neutrons for both single and double scattering. A novel SPAD has been developed specifically for the MONDO detector, called SPAD Based Acquisition, with time and spatial resolution tuned specifically for the experiment. Neutron energy resolution between 4% and 11% has been found for single scattering, while a resolution lower than $\sim 8\%$ has been found for double scattering events.

1.2.6 Weiming-1 CubeSat detector array

Weiming-1 is a compact, symmetrically structured detector array designed and developed for neutron detection using the recoil proton method. This innovative array comprises seven solid-state detectors (SSDs) and a hydrogen-containing conversion layer, effectively eliminating background noise from charged particles and gamma rays. The signals generated by recoil protons can be clearly distinguished, even in complex radiation environments, leading to improved accuracy in fast neutron flux measurements due to a higher signal-to-noise ratio. This advanced technology was used to construct a neutron spectrometer specifically designed for low Earth orbit applications, which was subsequently launched aboard the “Weiming-1” CubeSat at the beginning of 2024 [11].

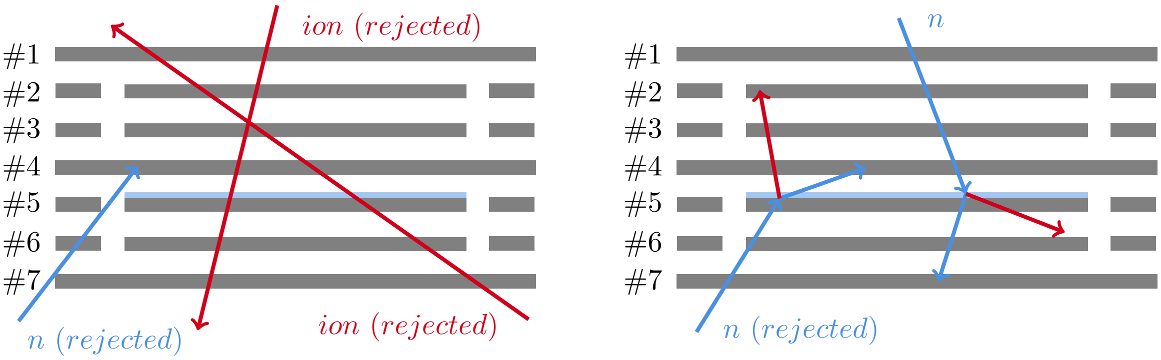

FIGURE 1.10: *Schematic drawings of signal classifications in Weiming-1: on the left events rejected by anti-coincidence detectors; on the right recoil protons generated by fast neutrons in the conversion layer.*

The detector array consists of seven silicon SSDs arranged coaxially as closely as possible, alongside a hydrogen-containing conversion layer (marked in blue), as shown in Figure 1.10. Detectors #1, #4, and #7 function as anti-coincidence detectors, while detectors #2, #3, #5, and #6 are segmented into inner and outer segments, labeled as A and B respectively. The hydrogen-containing conversion layer matches the area of the inner segment of the SSDs. The $\Delta E - E$ method can efficiently distinguish proton signals from other charged particles, applicable when particles with kinetic energy E traverse detector #5 and stop in detector #6. The energy E partitioning between these two detectors varies among particles due to their distinct stopping powers.

2 RecoIl Proton Track Imaging DEtector

In this chapter, a comprehensive discussion of the operational principles and design of the RIPTIDE detector is presented. The physical mechanisms for neutron detection by RIPTIDE are reviewed in Section 2.1. Detailed descriptions of its components are provided in Section 2.2, while Monte Carlo simulations are explained in Section 2.3.

2.1 Concept and working principle

In Chapter 1, an overview of the state-of-the-art fast neutron detectors was presented. The recoil proton track imaging technique, for both single and sequential n-p scattering, was discussed, highlighting its applications in neutron detection. Additionally, we described the three most significant detectors proposed for double n-p scattering recoil proton detection: SONTRAC, MONDO, and Weiming-1 CubeSat detector array. In this chapter, we discuss in detail the concept of the detector we aim to develop.

2.1.1 Concept

RIPTIDE, Recoil Proton Track Imaging Detector [19], is designed to detect neutrons in both single scattering mode and double scattering mode, with the differences discussed in Section 1.2.3. Unlike MONDO and SONTRAC, which utilize a matrix of scintillating fibers, RIPTIDE comprises a cube of plastic scintillator to overcome the spatial resolution limitations, since photons are produced along the entire proton track. Currently, while several systems are under investigation, no neutron tracker detector is in the data-taking phase.

The improvement in spatial resolution, however, is counterbalanced by the increased difficulty in optically capturing the photons. To address this challenge, the use of multiple optical systems is currently under evaluation. The proposed setup includes the use of two optical systems coupled to the scintillator to achieve stereoscopic imaging, facilitating a 3D reconstruction of the proton tracks within the scintillator. Additionally, a photo-multiplier is incorporated into the experimental setup to serve as a trigger and synchronize the optical systems for frame acquisition, ensuring simultaneous image capture. A conceptual sketch of RIPTIDE is shown in Figure 2.1.

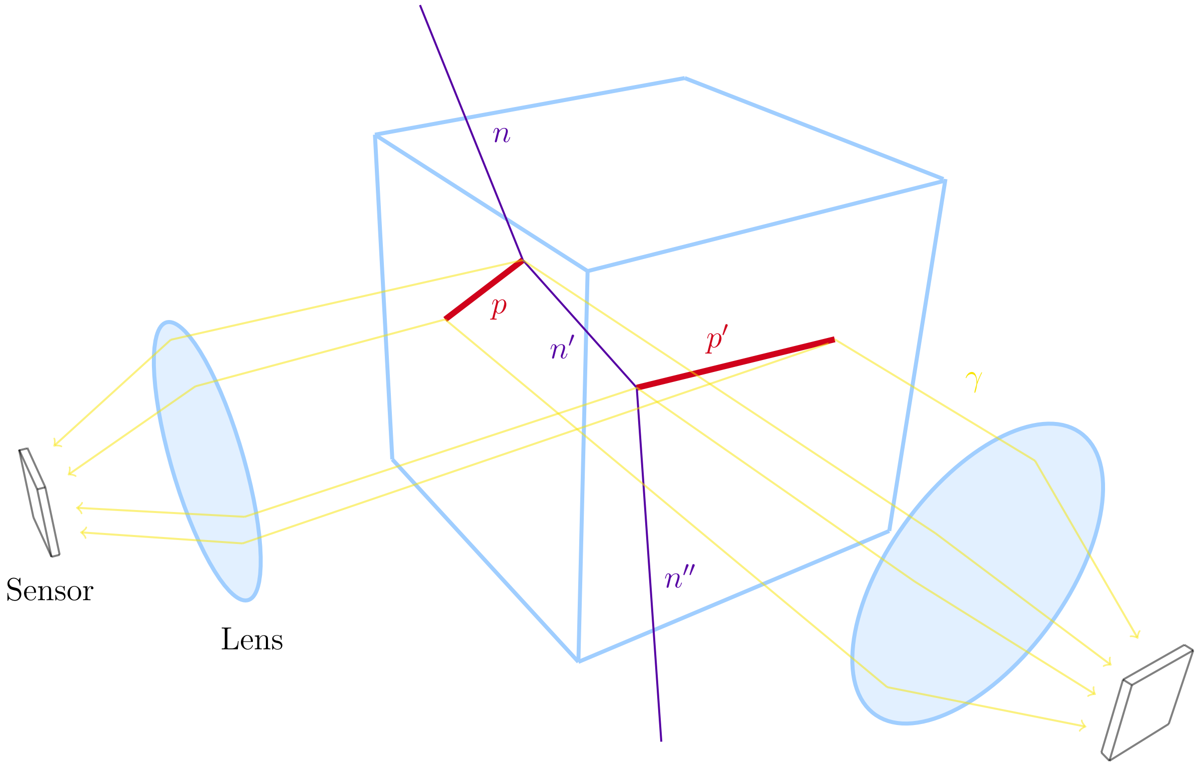

FIGURE 2.1: *RIPTIDE concept: a plastic scintillator is coupled to an optical system to acquire photons produced by recoil protons; a photo'multiplier will work as a trigger and synchronizer for the image acquisition from optical systems.*

RIPTIDE is designed to be versatile for various applications, as outlined in Section 1.1. As summarized in Table 2.1, several key requirements must be met to achieve scientific advances:

- The detection efficiency must reach at least 10%. It is important to note that the high efficiencies shown in Table 2.1 are achievable with the final detector. The current phase of the project is limited to the construction of a small prototype and to investigate the feasibility of a larger-scale experimental setup.
- The detector readout must be flexible to meet the specific experimental requirements. For example, dosimetry requires an inclusive readout with integration times

ranging from 0.01 to 1 s, while fast single-event readout is necessary for nuclear physics and particle therapy applications.

- For nuclear physics, it is crucial to achieve a very precise direction determination for neutron tracking.

	E (MeV)	Efficiency	S-o-A eff.	t res.	E res.	θ res.
Nuclear physics	10-100	0.1-0.6	-	1-10 ns	0.02-0.2	0.5°
Astrophysics	10-1000	0.1-0.5	0.1-0.3	1-100 ms	0.1-0.5	1°
Nuclear medicine	20-400	0.01-0.3	0.01-0.02	1-10 ns	0.05-0.2	0.5°
Agriculture	< 20	0.1-0.9	-	counter	-	1-5°

TABLE 2.1: *Requirements and expected region of interest in the different applications.*

Nuclear physics and particle therapy represent some of the most demanding applications in this field. In all instances, it is crucial to reject gamma and charged particle backgrounds. Background suppression can be effectively achieved on an event-by-event basis through dE/dx track characterization or by employing deep learning techniques to classify the tracks. Additionally, Monte Carlo simulations offer valuable insights for optimizing scintillator materials in terms of density, chemical composition, and light yield.

Implementing a first-level real-time trigger poses a significant challenge for a prototype detection system; however, it is essential for reducing data throughput. This reduction simplifies data transport and storage requirements, which is vital for on-field dosimetry and space applications.

2.1.2 Working principle

A neutron can only be detected if it interacts with the scintillator. However, due to the low cross section of nuclear interactions, the probability of such interactions is relatively low. As a result, most neutrons pass through the entire thickness of the scintillator without interacting, leading to undetected events. The active volume in RIPTIDE is comprises a plastic scintillator, primarily made of carbon and hydrogen. At the neutron energies of interest in the initial feasibility study for RIPTIDE, both neutrons and protons can scatter elastically. Neutrons can also interact with carbon either through elastic

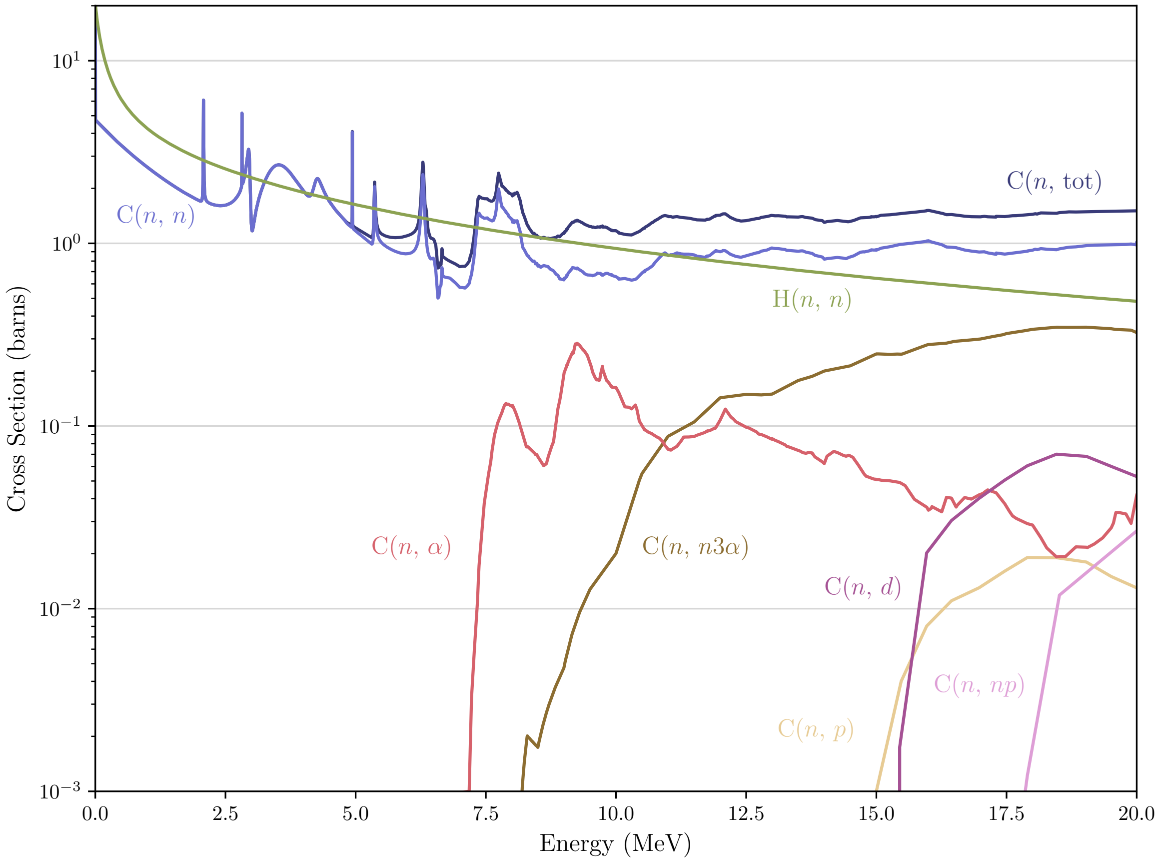

FIGURE 2.2: *Elastic and inelastic neutron cross section with carbon. Neutron-to-proton elastic scattering is also reported as a reference. Plotted data from ENDF/B-VIII.0* [4].

scattering or nuclear reactions, with the probability of the latter increasing with neutron energy. Figure 2.2 displays the experimental values of the main reactions occurring within the scintillator volume.

A neutron can only be detected if it interacts with the scintillator. However, due to the low cross section of nuclear interactions, the probability of such interactions is relatively low. As a result, most neutrons pass through the entire thickness of the scintillator without interacting, leading to undetected events. The active volume in RIPTIDE comprises a $6 \times 6 \times 6$ cm^3 plastic scintillator, primarily made of carbon and hydrogen. At the neutron energies of interest in the initial feasibility study for RIPTIDE, both neutrons and protons can scatter elastically. Neutrons can also interact with carbon through either elastic scattering or nuclear reactions, with the probability of the latter increasing with neutron energy. Figure 2.2 displays the experimental values of the main reactions occurring within the scintillator volume.

In a collision, a neutron transfer part of its energy to the nucleus involved in the interaction. The amount of transferred transferred depends on the atomic number A of the nucleus and is uniformly distributed as follows:

$$E \in \left[\left(\frac{A-1}{A+1} \right)^2 E_n^{(1)}, E_n^{(1)} \right], \tag{2.1.1}$$

where $E_n^{(1)}$ is the neutron energy before the interaction.

If a neutron interacts once or twice with protons, its energy and direction can be determined, as discussed in Section 1.2.3. Stereoscopic imaging is employed to obtain the proton track. All the information necessary for recoil proton track imaging (RPTI) can be derived from these proton tracks, which appear as segments with one end brighter than the other due to energy loss, indicative of the proton direction of movement, as described by the Bragg curve.

However, the experimental signature of neutron-carbon elastic scattering is often below the detection threshold, which adversely affects detection efficiency. For instance, a neutron may first interact with a carbon nucleus before interacting with a proton. In this initial interaction, both the neutron kinetic energy and direction are altered. This first interaction may not be detectable by the optical system, while the subsequent interaction with the proton might be. As a result, the double scattering event could be misinterpreted as a single scattering event, leading to an incorrect calculation of the neutron initial energy.

2.2 Detector components

With the principle of operation of RIPTIDE established, we can now examine its key components, each of which plays a role in neutron detection. The scintillator detects neutron interactions by converting energy into light. The detector readout processes these light signals for data extraction. The trigger system optimizes event recording, while the electronics handle signal amplification and transmission.

2.2.1 Scintillator

The plastic scintillator used in RIPTIDE is BC-408, composed of polyvinyl-toluene. This scintillator is characterized by its excellent time resolution, with fast rise and decay times

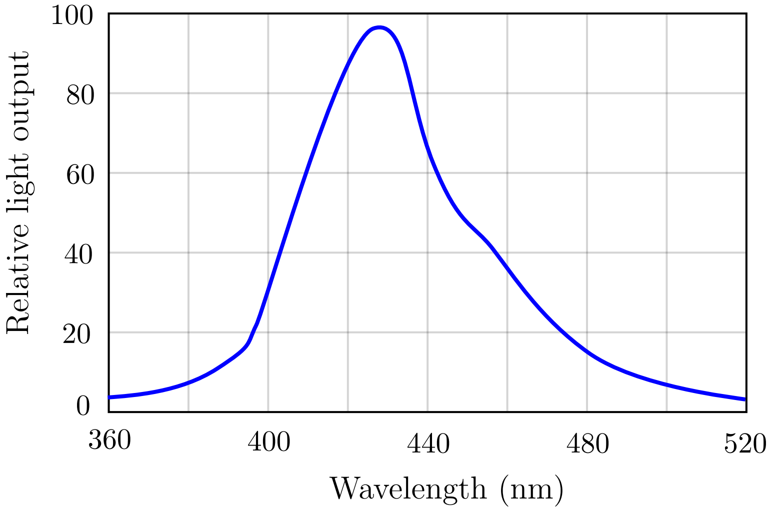

Figure 2.3: *Emission spectrum of BC-408 plastic scintillators. The spectrum is peaked around 430 nm, in the blue-violet region.*

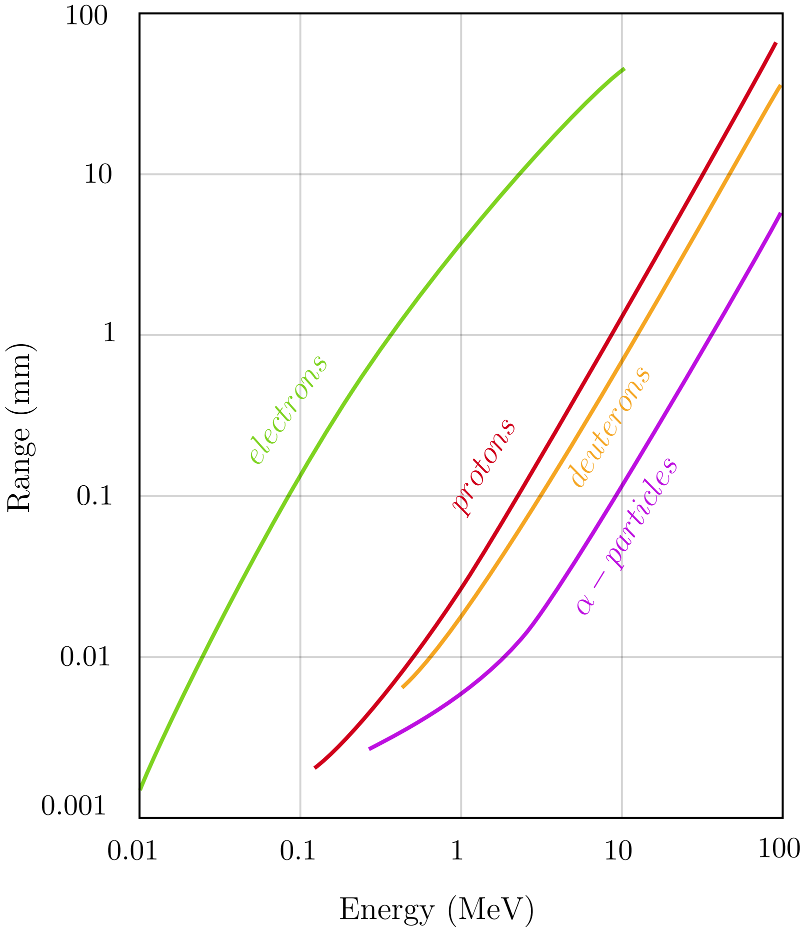

Figure 2.4: *Range of different particles in BC-408 plastic scintillator. In our region of interest, proton range is between 0.2 and 30 mm.*

of 0.9 ns and 2.1 ns, respectively. Additionally, it has a favorable proton-to-carbon ratio, approximately equal to one.

The scintillator emits light peaking at 430 nm, within the blue-violet spectral range. It is crucial to account for this wavelength when coupling with the optical system. The emission spectrum (see Figure 2.3) must overlap with the readout system acquisition spectrum to ensure effective detection. A cubic scintillator with dimensions of $6 \times 6 \times 6$ cm^3 was selected. Figure 2.4 shows the proton range as a function of its energy within the BC-408 plastic scintillator.

2.2.2 Detector readout

The optical system is a critical component in the detector design, requiring extremely high spatial resolution and photon detection efficiency. Currently, two types of setups are under investigation. The first setup utilizes only a back-illuminated CMOS sensor, which offers several advantages over CCD sensors, including better noise performance and higher sensitivity. However, given the extremely low-light conditions encountered, a second setup is also being explored that combines the CMOS camera with a microchannel plate (MCP) image intensifier. This combination amplifies the signal, enabling the system to achieve the required performance in detecting faint signals.

The first type of setup is based only on a CMOS sensor. CMOS sensors have recently surpassed CCDs in scientific research for visible and ultraviolet imaging due to their compact size, lower power consumption, and greater radiation tolerance. Unlike CCDs, which transfer charge sequentially to a common output structure, CMOS sensors perform charge-to-voltage conversion simultaneously within each pixel. This fundamental difference enables more efficient and faster image acquisition. Back-illuminated CMOS sensors, illuminated from the back of the silicon substrate, offer significantly improved sensitivity compared to front-illuminated sensors. The optical system under study, illustrated in Figure 2.5, utilizes a back-illuminated CMOS sensor. This system exhibits high quantum efficiency in the emission wavelength range of the scintillator, making it well-suited for use with the BC-408 scintillator without significant efficiency loss.

The complementary optical system under study also involves microchannel plates (MCPs), which provide high spatial resolution and a large detection surface. MCPs, commonly used in similar configurations for electron track reconstruction, can achieve real-time acquisition with a time resolution of 100-200 ps. The system, illustrated in

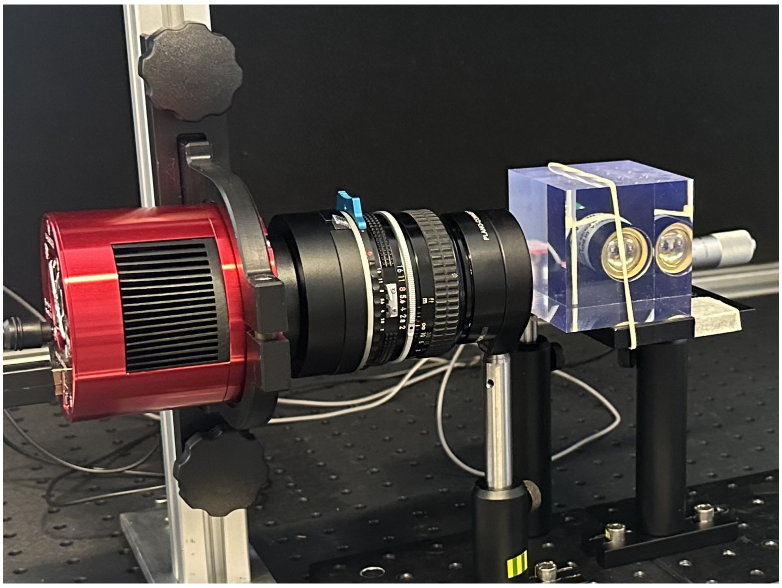

Figure 2.5: *The first setup utilizes a back-illuminated CMOS sensor, specifically the ASI 533MM PRO. In this configuration, the scintillator cube is visible, accompanied by a photomultiplier tube (PMT) that serves as a trigger for detecting light signals.*

Figure 2.6, comprises a photon-to-electron converter, an electron amplifier, and an electron readout system. MCPs consist of numerous tiny pores coated with a semiconductor

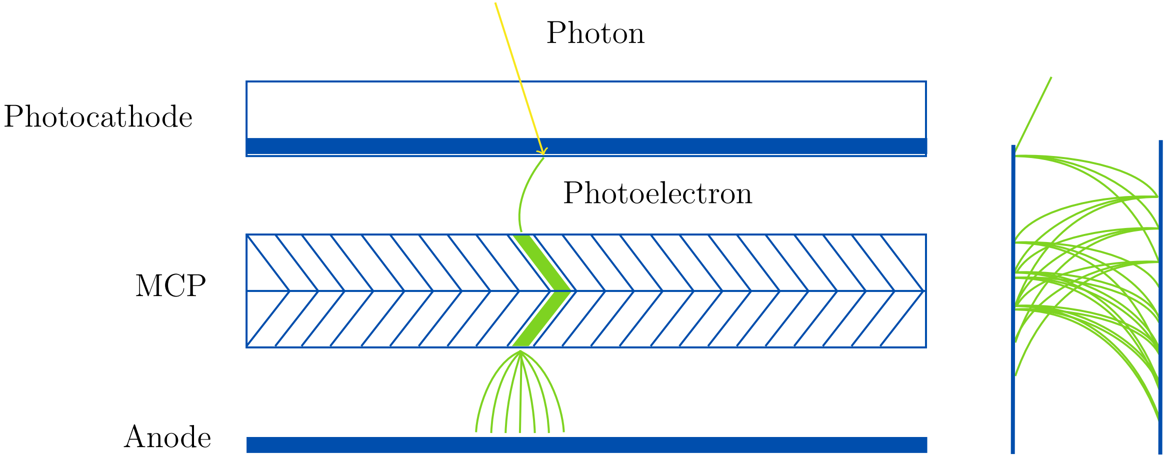

Figure 2.6: *Working principle of the MCP.*

material, where incoming electrons are accelerated and multiplied, resulting in an electron cloud that can amplify the signal by a factor of 10^3 to 10^7. This amplified electron cloud is then detected by high spatial resolution detectors. Notably, the CMOS camera remains in the setup, capturing amplified images of the MCP output screen.

2.2.3 Trigger

The development of the trigger system involves the creation of two distinct setups. The first setup incorporates a photomultiplier tube (PMT), as depicted in Figure 2.5. In this configuration, the PMT covers an entire face of the scintillator cube, thereby making that face unavailable for image acquisition. The second setup employs a silicon photomultiplier (SiPM), offering a more compact design due to its smaller size and enabling image acquisition from the face of the cube where the photomultiplier is situated.

The fundamental concept of the trigger system revolves around the utilization of an external fast trigger to provide a time reference for synchronizing the cameras that capture stereoscopic images. This approach involves pausing image acquisition when the photomultiplier detects a signal, allowing for precise identification of the relevant frames for subsequent analysis.

2.2.4 Electronics

The electronics of the RIPTIDE detector, built around a highly programmable System-on-a-Module (SOM) board, are designed to manage high data input rates from both trigger detectors, which can be either Silicon Photomultipliers (SiPMs) or Photomultiplier Tubes (PMTs), and the imaging cameras. The SOM board, featuring an FPGA and an embedded ARM CPU, processes digitized signals from the trigger detectors to tag relevant frames, while simultaneously handling data from the cameras, with input rates ranging from 1 MB/s to 10 GB/s, depending on the level of sparsification provided by the sensors.

The FPGA performs real-time noise subtraction and feature extraction, identifying frames that indicate potential neutron interactions. When non-empty frames are detected from multiple sensors or a coincidence is observed in the trigger detector signals, the embedded CPU initiates further data processing. The system supports up to four independent channels, storing time-tagged frames in a circular RAM buffer. Triggered frames are then extracted and transferred to storage via a 1 Gbps Ethernet connection.

2.3 The Monte Carlo dataset

2.3.1 Geant4 simulation

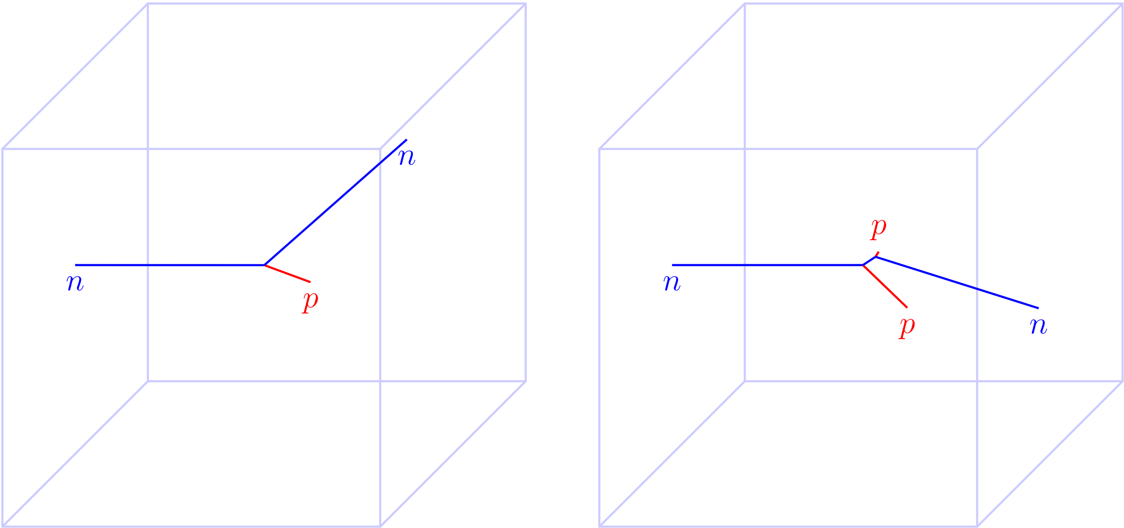

(A) *Single scattering event.*

(B) *Double scattering event.*

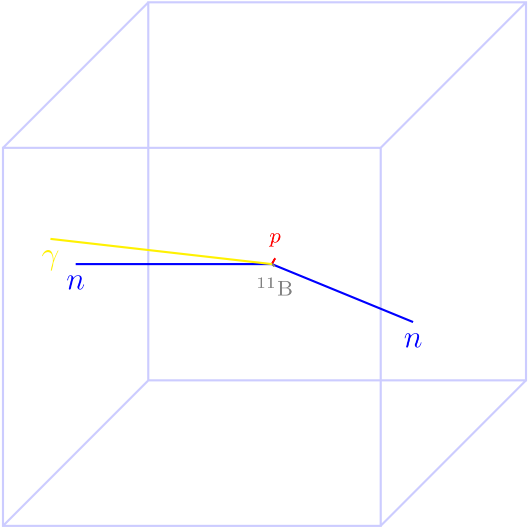

(C) *An example of background event.*

FIGURE 2.7: *Simulated scattering events within the cubic scintillator, showing different types of particle interactions and their trajectories. The events include single* (A) *and double* (B) *scattering. The third event* (C) *depicts an example of a background event.*

The detection concept has been supported through Monte Carlo simulations based on the Geant4 toolkit [1], version 11.4.1. The scintillation cube (of size $6 \times 6 \times 6$ cm^3) has been described with a composition of plastic polyvinyl-toluene. The properties of the specific material have been considered representative of the BC-408 and have been retrieved from the NIST database [22] available among the code libraries: composition name is `G4_PLASTIC_SC_VINYLTOLUENE`, with stoichiometric ratio C/H $= 9/10$, density 1.032 g/cm^3 and ionization energy of 64.7 eV. Transport simulations by Geant4 have been ruled by standard physics lists based on models. In particular, neutron-proton interaction has previously been tested within the framework of other experiments and it is considered as validated in this context and reliable in the current energy range. Moreover, the optical photon production and transportation features of Geant4 have been enabled. In fact, suitable physics libraries are available to be used together with proper material characteristics to be defined. In accordance to the BC-408 data sheet [23], a number of 10^4 optical photons per MeV were produced along the proton track and transported inside the plastic scintillator. In addition, a refractive index of 1.59 has been considered as well as a very long absorption length, compared to the cube dimension. In this way, the photons can be originated along the tracks of charged particles, mainly protons, ionizing the scintillator. Then they are emitted uniformly into the 4π solid angle with a random linear polarization perpendicular to their momentum direction.

In the simulation, one million monoenergetic neutrons with an energy of 100 MeV were generated just outside the scintillator cube, along the positive x-axis direction. From this dataset, events of interest were selected, specifically those where a neutron produced either a single (see Figure 2.7a) or double (see Figure 2.7b) proton recoil within the scintillator. To ensure clear track visibility on the sensor, only protons with kinetic energies greater than 40 MeV were considered in the analysis. This energy threshold guarantees that the proton tracks are sufficiently distinct and detectable. Background events (see Figure 2.7c) were excluded from the analysis.

```
********************************************************************************************************************************
 event   * track * particle * parent * energy *  v_x    *  v_y    *  v_z    * v_dir_x * v_dir_y * v_dir_z * end_x   * end_y   * end_z   * distance
********************************************************************************************************************************
 678607 *     1 *  neutron *      0 *    100 *   -550 *       0 *       0 *       1 *       0 *       0 *     500 *-84.791 * 76.839 * 1056.216
 678607 *     3 *   proton *      1 * 40.318 * 32.427 * 15.853 *-15.735 *   0.295 *   0.683 *  -0.667 * 37.239 * 25.741 *-25.377 *   14.625
 678607 *     2 *   proton *      1 * 41.405 * 5.1258 *       0 *       0 *   0.653 *  -0.537 *   0.533 * 15.243 * -8.327 *  7.744 *   15.221
```

FIGURE 2.8: *Informations provided by Geant4 in a simulated event.*

All simulated event data is organized in three `ROOT::TTree` structures [5]. The first tree, `RIPTIDE_particle`, stores information about the tracks of all particles involved in each event as shown in Figure 2.8. The second tree, `RIPTIDE_photons`, records all optical photons emitted by charged particles as they traverse the scintillator. Finally, `RIPTIDE_events` aggregates high-level information about the content of each event, offering a summary of key characteristics such as the number of particles and interactions. Together, these trees allow for a detailed reconstruction and analysis.

2.3.2 Scintillation light propagation through the optical system

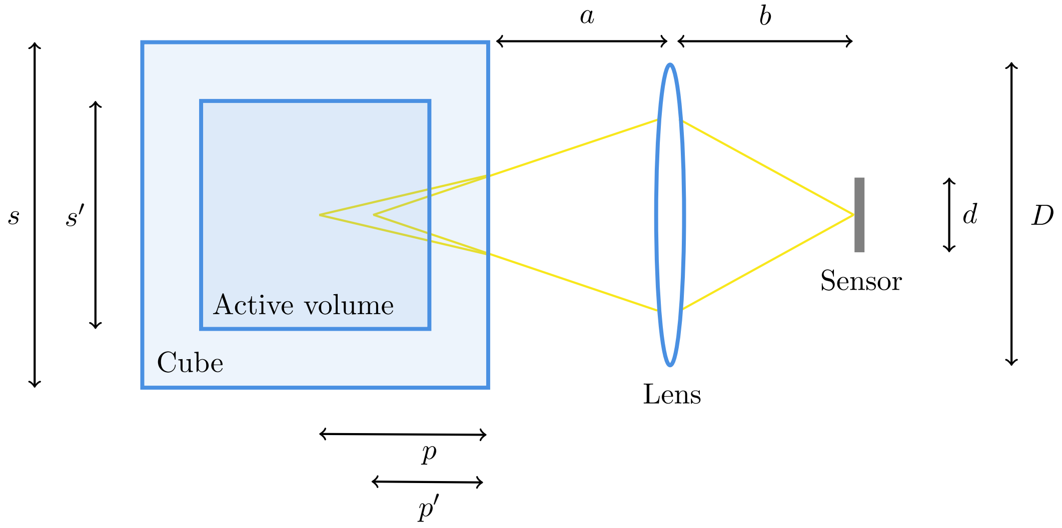

FIGURE 2.9: *Sketch of a simple setup for the simulation of optical photon transport.*

The simulation code, developed in Geant4 and discussed in the previous section, is designed to track the optical photons generated by charged particle tracks within the scintillator cube. The primary aim is to record the starting points and directions of these optical photons, which are then saved in data files. A custom code subsequently simulates the propagation of these photons from their point of generation to the sensor. The sensor captures a 2D projection of one face of the scintillator cube.

We simulated the response of a simple optical system made of a lens and a large surface sensor to maximize the photon collection efficiency. This simple case, sketched in Figure 2.9 allowed us to study the propagation of photons, including light refraction and aberrations. As mentioned above, in the Geant4 simulations, an inner active volume for the proton detection with side 40 mm (s' in Figure 2.9) was considered. Lens and sensor parameters were set in a way to cover the whole active volume. By considering a realistic sensor size of 20 mm (d in Figure 2.9), a magnification factor of 0.5 was chosen. The remaining parameters were determined based on these constraints using the thin lens equation and Snell's law, with a refractive index of $n = 1.59$ for the interface between

```
CubeSide                100 # mm
ScintillatorIndex      1.59
LensDistance         311.13 # mm
FocalLength             100 # mm
LensRadius               30 # mm
SensorDistance       461.13 # mm
SensorSide               20 # mm
```

FIGURE 2.10: *Run conditions configuration file contains key parameters defining the geometry of the detector.*

the scintillator and air. These input parameters are supplied to the simulation through a configuration file, an example of which is shown in Figure 2.10.

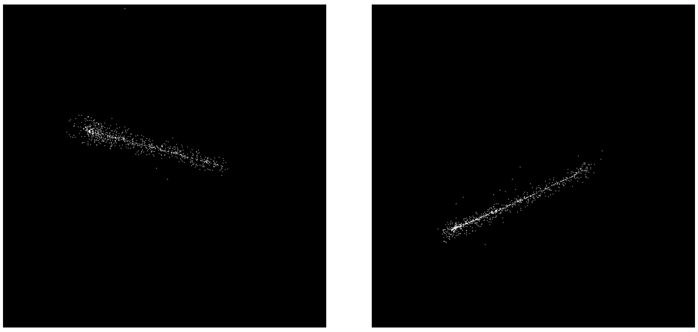
(A) *(xz) projection.* (B) *(xy) projection.*

FIGURE 2.11: *Projections of a single proton track on the sensor.*

The propagation of photons through this simple optical setup introduces various types of aberrations, with spherical and comatic aberrations being the most significant. Spherical aberration occurs when photons passing through the edges of the lens are refracted more than those passing near the center, leading to a blurry image as light rays converge at different focal points. Comatic aberration, or coma, produces asymmetrical distortion, typically in off-axis points, causing images of point sources to appear as comet-like streaks rather than sharp dots.

In addition to these optical aberrations, depth of field (DOF) effects also contribute to image degradation. When the object being imaged (in this case, the proton track) extends over a range of depths, only a portion of it can remain sharply in focus, while parts outside the DOF appear blurred. This introduces further noise into the imaging process, complicating the reconstruction of accurate track lengths from the sensor images.

The simulation generated 2D projections for each face of the scintillator cube, with the sensor positioned at a distance of $a + b$ from the outer surface of the BC-408 cube, as illustrated in Figure 2.9. For our analysis, we focused on two specific projections, which are presented in Figure 2.11. These projections are in graylevel, with the intensity values proportional to the number of photons reaching the sensor. These 2D images, each measuring 256×256 pixels, serve as the input for the subsequent analysis.

3 | Imaging reconstruction techniques

In this chapter, the techniques used to determine the direction, orientation, and length of proton tracks projections in the sensor are presented. As illustrated in Figure 1.7 and Figure 1.8, accurately extracting the characteristics of the proton track projections from its photograph is the first step in reconstructing the energy and momentum of the incident neutron. The methods for determining direction and orientation are explained first followed by the process for calculating track length. The process includes the application of deep learning techniques to correct optical aberrations and subsequently reconstruct the track length on the sensor.

3.1 Track reconstruction: direction and orientation

This analysis aims to determine both the direction and orientation of the track projections on the sensor. The Hough transform is employed to identify straight-line features in the images by converting pixel coordinates into polar coordinates, where lines correspond to peaks in the Hough space accumulator. Through discretization, the method detects the best-fit line representing the track projection on the sensor. To determine the track orientation, the analysis first computes the track barycenter, translates the coordinate system to center around it, and then rotates the system by the identified angle. Finally, the skewness of the grayscale pixel distribution, which follows the Bragg peak, is used to confirm the correct orientation of the track.

3.1.1 Hough transform for direction

The Hough transform [9] is a widely used technique for extracting geometric features in images, particularly valued for its robustness against random noise. Originally developed for detecting particle trajectories in bubble chambers, the Hough transform has since become a fundamental tool in computer vision, with its simplest and most common application being the detection of straight lines. This method identifies lines by transforming points in the image space into a parameter space, where lines correspond to peaks in the Hough space accumulator. Given the method's robustness in noisy environments and its adaptability to various geometrical shapes, it has been chosen for our analysis. Although the Hough transform is often used to detect multiple lines in complex images, for simplicity, we will limit its application to the case of single proton trajectories.

Let w and h denote the width and height of the photograph, respectively, where the image space origin is set at the top-left corner. As illustrated in Figure 3.1, each pixel (x, y) in the photograph can be parametrized in terms of polar coordinates (θ, ρ), where $\theta \in [0, \pi)$ and $\rho \in \left[-\sqrt{w^2+h^2}/2, \sqrt{w^2+h^2}/2\right]$. The relation between the pixel coordinates (x, y) and the corresponding parameters (θ, ρ) is given by the well-known equation of a straight line in the Hough transform:

$$\rho = \left(x - \frac{w}{2}\right)\cos\theta + \left(y - \frac{h}{2}\right)\sin\theta. \tag{3.1.1}$$

In this form, θ represents the angle of the normal vector to the line relative to the x-axis, while ρ is the perpendicular distance from the origin of the image space to the line. For each pixel (x, y) that belongs to a line in the image space, this equation maps the pixel to a sinusoidal curve in the Hough space.

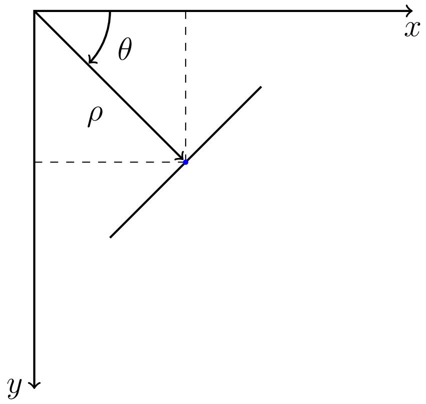

FIGURE 3.1: *Hough transform with (θ, ρ) parametrization, used to detect and characterize straight-line features in the image space by mapping them into polar coordinates.*

By discretizing both θ and ρ into a finite number of bins ($\delta\theta = 1°$ and $\delta\rho = 1$ pixel), an accumulator matrix is created, where each point (x, y) in the image contributes a curve in the Hough space. The peak in this accumulator matrix correspond to values of (θ_p, ρ_p) that are consistent with the presence of a line in the photograph. Furthermore, by applying the inverse Hough transform, it is possible to retrieve the equation of the detected line in the original image space. Given a peak at (θ_p, ρ_p) in the Hough accumulator, we can determine the corresponding line equation by solving for the pixel coordinates that satisfy the line equation in Cartesian space.

The procedure described above is illustrated step by step in Figure Figure 3.2. In Figure 3.2a, we observe the projection of the particle track onto the $+xy$-plane, which represents the input to the Hough transform. This image shows the raw trajectory data captured by the sensor. In Figure 3.2b, the corresponding Hough accumulator is displayed, where each point in the original image contributes a sinusoidal curve based on the parameterization. The accumulator is filled by applying the Hough transform equation to the pixel coordinates of the track projection. Finally, in Figure 3.2c, the result of the Hough transform is shown. The peak in the accumulator, corresponding to the highest vote count, provides the optimal parameterization which best defines the straight-line representation of the trajectory in the image space.

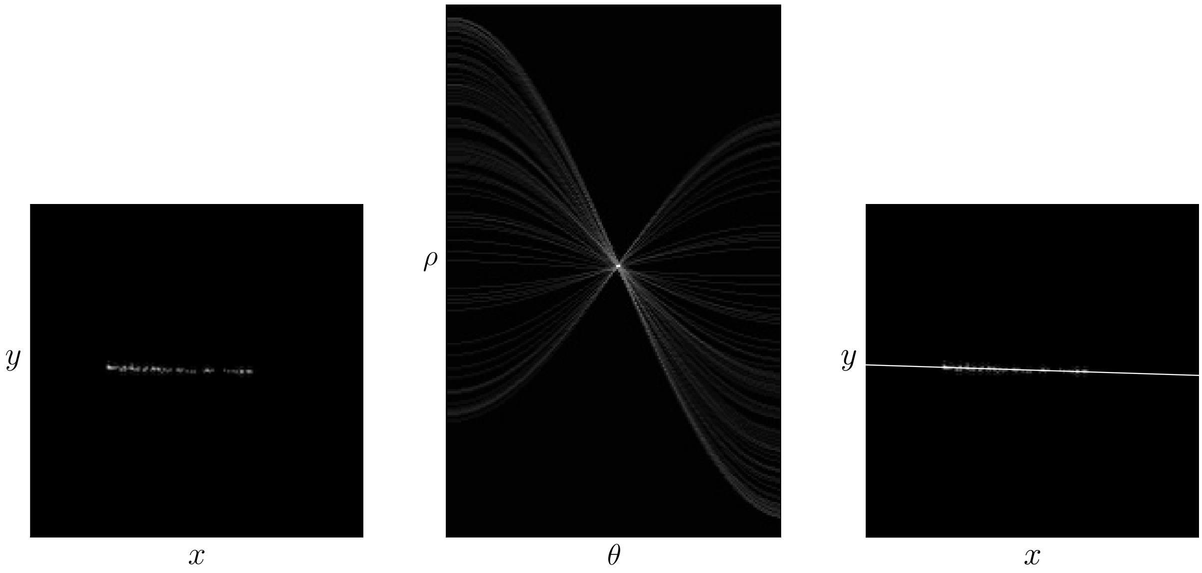

(A) *Track projection.* (B) *Hough accumulator.* (C) *Hough transform result.*

FIGURE 3.2: *Hough transform steps:* (A) *$+xy$ track projection on the sensor;* (B) *the accumulator is filled by applying Equation 3.1.1 on the previous projection;* (C) *the accumulator peak provides the best parametrization of the projection.*

The angle θ_p represents the direction of the detected track projection in the image space. The results of this analysis will be presented in the following chapter (Section 4.1.1). From this point onward, we will denote the direction obtained via the Hough transform as θ_p, which will be referenced in the following sections as a key parameter.

3.1.2 Momenta analysis for orientation

In the previous section we showed how to determine the track direction on the sensor using the Hough transform. The analysis will now proceed with determining the track orientation by using the fact that the energy loss of the proton within the scintillator follows a specific pattern: the Bragg curve.

The initial step in the analysis of momenta involves computing the barycenter of the projected track on the sensor. The barycenter is determined using the following equations for the x and y coordinates:

$$x_b = \frac{\sum_i w_i x_i}{\sum_i w_i}, \quad y_b = \frac{\sum_i w_i y_i}{\sum_i w_i}, \tag{3.1.2}$$

w_i denotes the grayscale of the pixel in the coordinate (x_i, y_i). The second step involves setting the barycenter as the origin of our coordinate system, allowing us to express the positions of all points relative to this central reference. This coordinate transformation

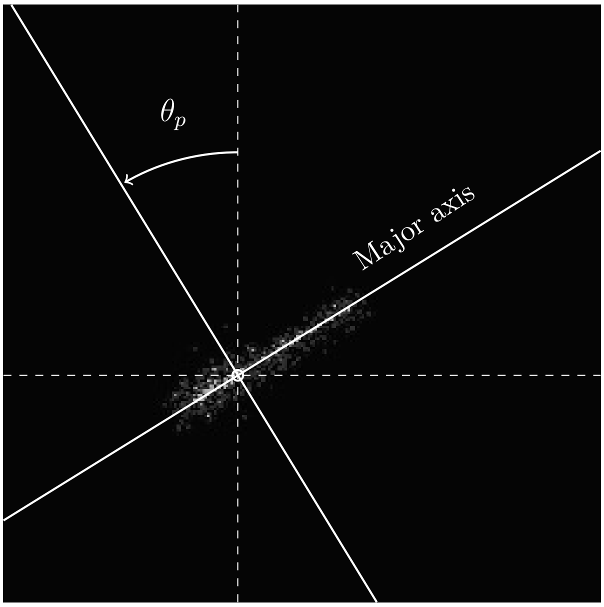

FIGURE 3.3: *Representation of the steps in momenta analysis. First, the barycenter is identified, and the origin of the coordinate system is translated to the barycenter, then the axes are rotated by an angle* θ_p.

is defined as:

$$x_i \to x_i - x_b, \quad y_i \to y_i - y_b. \tag{3.1.3}$$

The third step is to rotate the coordinate system by the angle θ_p:

$$\begin{pmatrix} x'_i \\ y'_i \end{pmatrix} = \begin{pmatrix} \cos\theta_p & -\sin\theta_p \\ \sin\theta_p & \cos\theta_p \end{pmatrix} \begin{pmatrix} x_i \\ y_i \end{pmatrix}, \tag{3.1.4}$$

which is determined using the Hough transform. This rotation aligns one of the reference frame axes with the track direction, which we define as the *major axis*. In Figure 3.3 the previous steps are represented on a track photograph.

The final step involves calculating the skewness of the grayscale pixel distribution projected along the major axis (see Figure 3.4) using:

$$\mu_3 = \frac{\sum_i w_i x_i'^3}{\sum_i w_i} = \frac{\sum_i w_i (x_i \cos\theta_p + y_i \sin\theta_p)^3}{\sum_i w_i}, \tag{3.1.5}$$

where the distribution follows the Bragg peak. The skewness provides information about the relative location of the Bragg peak with respect to the barycenter. Specifically, if $\mu_3 < 0$, it indicates that the reconstructed angle θ_p aligns with the orientation of the Bragg peak. On the other hand, if $\mu_3 > 0$, it suggests that the direction is reversed, and thus should be adjusted to $\theta_p \to \theta_p + \pi$.

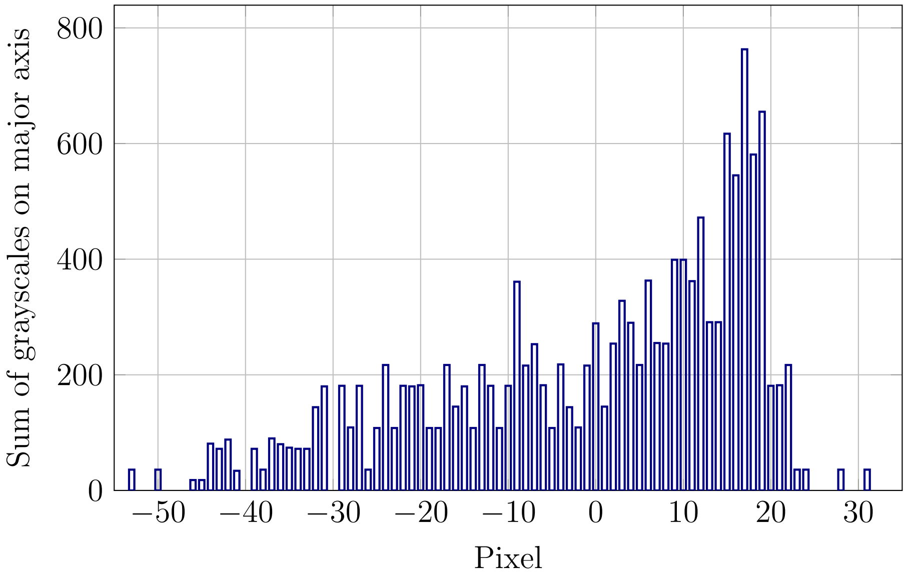

FIGURE 3.4: *Plot illustrates the summed grayscale distribution along the major axis. The distribution follows the profile of the Bragg peak.*

This method clearly requires that the projected tracks on the sensor have a sufficient length to exhibit the Bragg peak pattern. The results of this analysis will be presented in the next chapter (Section 4.1.1).

3.2 Track reconstruction: length

3.2.1 Removing optical aberrations

The optical system of the detector, as detailed in Section 2.3.2, introduces optical aberrations that cause non-quantifiable errors in the reconstructed projected track length on the sensor. These aberrations reduce the precision of the track length reconstruction.

To mitigate these optical aberrations and enhance the accuracy of track length reconstruction, a deep learning-based approach was employed. Convolutional Neural Networks (CNNs) [15] are used for image processing tasks due to their ability to extract relevant features through the application of translationally invariant filters. By learning to correct the distortions caused by the optical system, this approach can compensate the lens-induced aberrations.

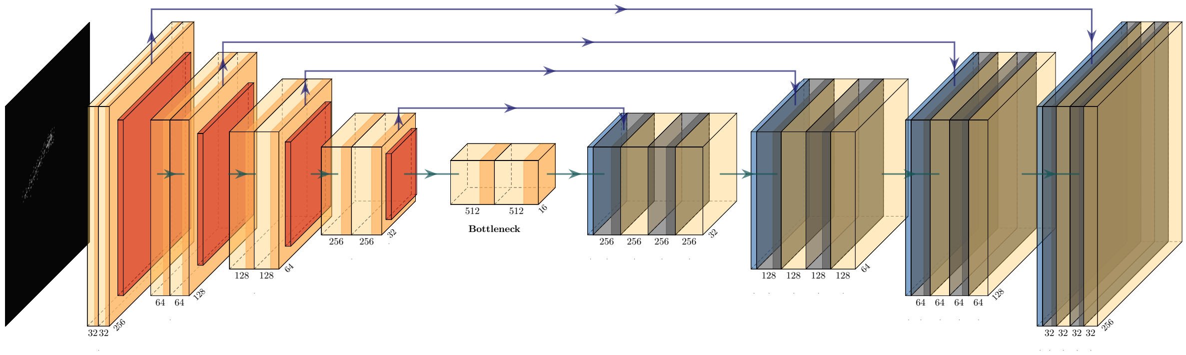

Figure 3.5: *Visual representation of a U-Net, which uses concatenation to combine feature maps from downsampling and upsampling layers.*

The architecture developed for our problem is a U-Net model [20] (see Figure 3.5). A key aspect of the U-Net design is the use of skip connections, which link layers from the contracting path to corresponding layers in the expanding path. In the U-Net, these skip connections are implemented via concatenation, where feature maps from downsampling layers are directly appended to the upsampling layers feature maps. This preserves the complete set of feature maps, ensuring that the high-resolution features from earlier layers are not lost.

Skip connections, as introduced in ResNet [13], play a crucial role in deep neural networks by addressing the vanishing gradient problem [14] and improving information flow between layers. In our model, we maintain the standard U-Net approach by utilizing concatenation for the skip connections, which ensures that both low-level and high-level features are retained and combined effectively in the upsampling stages. The model architecture, including the implementation of skip connections, is detailed in the code provided in Figure 3.7 (written using TensorFlow 2.16 with Keras 3 [7]).

The network is provided with two types of images, both with resized dimensions of `(256, 256, 1)`. The first image (Figure 3.6a) shows the proton track as it appears on the sensor, including distortions caused by the optical system. The second image (Figure 3.6b) is a simplified representation: a straight line connecting the proton start and end points. This second image lacks directional information about the proton orientation, but it preserves the length of its path. This simplification facilitates feature extraction.

(A) *Aberrated track on sensor.* (B) *Proton track segment.*

FIGURE 3.6: *The training dataset consists of two images: the first shows an aberrated proton track as projected onto the sensor* (A)*, while the second represents the idealized proton track segment without any orientation information* (B)*.*

During the training phase, the model is trained to minimize the reconstruction error using an exponential decay learning rate schedule. The learning process starts with an initial learning rate of 0.01, which gradually decreases by a factor of 0.9 at specific intervals. This decay schedule allows the model to make larger updates in the early stages of training and smaller, more refined updates as the training progresses, helping

```
def double_conv_block(x, n_filters):
  x = Conv2D(n_filters, 3, padding="same", activation="relu", kernel_initializer="he_normal")(x)
  x = Conv2D(n_filters, 3, padding="same", activation="relu", kernel_initializer="he_normal")(x)
  return x

def downsample_block(x, n_filters):
  conv_output = double_conv_block(x, n_filters)
  pooled_output = MaxPool2D(2)(conv_output)
  pooled_output = Dropout(0.3)(pooled_output)
  return conv_output, pooled_output

def upsample_block(x, skip_connection, n_filters):
  x = Conv2DTranspose(n_filters, 3, strides=2, padding="same")(x)
  x = concatenate([x, skip_connection])
  x = Dropout(0.3)(x)
  x = double_conv_block(x, n_filters)
  return x

def unet_model():
  inputs = Input(shape=(256, 256, 1))

  conv_block1, pool_block1 = downsample_block(inputs, 32)
  conv_block2, pool_block2 = downsample_block(pool_block1, 64)
  conv_block3, pool_block3 = downsample_block(pool_block2, 128)
  conv_block4, pool_block4 = downsample_block(pool_block3, 256)

  bottleneck_block = double_conv_block(pool_block4, 512)

  upsample_block1 = upsample_block(bottleneck_block, conv_block4, 256)
  upsample_block2 = upsample_block(upsample_block1, conv_block3, 128)
  upsample_block3 = upsample_block(upsample_block2, conv_block2, 64)
  upsample_block4 = upsample_block(upsample_block3, conv_block1, 32)

  output_layer = Conv2D(1, 1, padding="same", activation="linear")(upsample_block4)

  model = Model(inputs, output_layer, name="U-Net")
  return model
```

FIGURE 3.7: *U-net architecture details.*

to stabilize the learning process and prevent overshooting the optimal solution.

Additionally, an early stopping mechanism is applied to monitor the validation loss. If the validation loss does not improve for 5 consecutive epochs, training is stopped early to prevent overfitting. The best-performing model weights, based on the lowest validation loss, are restored at the end of the training. This ensures that the final model is the one that generalizes best to unseen data, as measured by the validation set.

The model is compiled using the *RMSprop* optimizer, which is well-suited for tasks with noisy gradients like this one. The loss function chosen is Mean Squared Error (MSE), which is appropriate for this regression task, where the goal is to predict continuous values such as the length of the proton track. The behaviour of the loss function during epochs is reported in Figure 3.8.

The training runs for a maximum of 30 epochs, with a batch size of 8. Validation is performed using a test set at the end of each epoch, and the model is regularly evaluated on unseen data to ensure generalization.

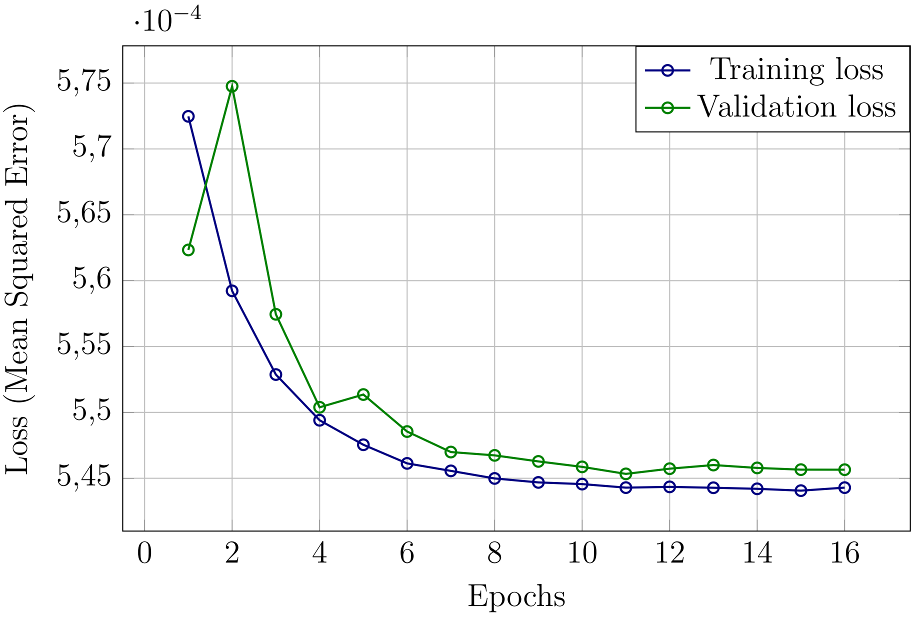

FIGURE 3.8: *Behaviour of the loss function, in our case Mean Squared Error, during the epochs.*

During the inference phase, the trained model is applied to new, unseen data to make predictions, as shown in Figure 3.9. At this stage, the model weights are frozen, and it utilizes the learned transformations to reconstruct proton track lengths from the input images. The main goal of this phase is to assess the model ability to generalize to previously unseen data. As we can see in Figure 3.9b, the model accurately reconstructs the track segment, significantly improving the precision of the track endpoints compared to the aberrated track. This demonstrates the model ability to correct for distortions and provide more reliable reconstructions.

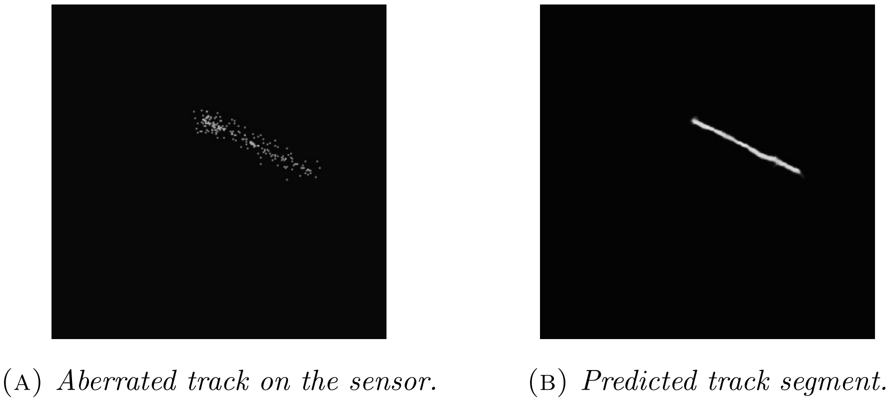
(A) *Aberrated track on the sensor.* (B) *Predicted track segment.*

FIGURE 3.9: *The inference phase applies the trained model to new, unseen data to reconstruct proton tracks. This figure shows an example of an aberrated input track* (A)*, the corresponding prediction from the model* (B)*.*

3.2.2 Length estimation

To estimate the length of an unaberrated projected track, we can sum the non-zero pixels along each axis of the image, corresponding to the track segment (see Figure 3.10). By identifying the starting and ending points of the non-zero pixels, we can determine in a very simple way the length of the track in pixels. The relationship between the physical length of the track (in millimeters) and its representation on the sensor (in pixels) is given by the following equation:

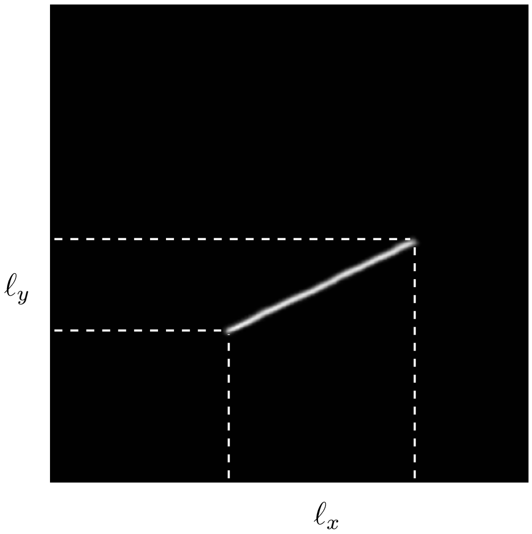

FIGURE 3.10: *Schematic representation of the track length estimation process.*

$$\text{length [mm]} = \left(\frac{\text{cube side [mm]}}{\text{sensor side [pixels]}} \right) \text{length [pixels]} \tag{3.2.1}$$

Results concerning the 3D track lengths, specifically the proton ranges within the scintillator, reconstructed from two orthogonal projections, will be presented in the following chapter (Section 4.1.2).

4 | Neutron energy and momentum

The aim of this chapter is to present the results obtained from the image analysis techniques developed and outlined in Chapter 3 for Monte Carlo image analysis. The results related to the reconstruction of the direction and orientation of 3D proton tracks from the two sensor projections, as illustrated in Figure 2.11, are detailed. Additionally, the outcomes of proton range reconstruction, from which the proton energy is inferred, are discussed. Finally, using Equation 1.2.1, the energy of neutrons undergoing single scattering is reconstructed. Moreover, it is demonstrated how the procedure applied to the single-scattering case can be generalized to double scattering. Since this analysis is still ongoing, a preliminary outline of the future developments will be provided.

4.1 Single scattering reconstruction

4.1.1 Direction and orientation results

In this section, we discuss the results obtained from the reconstruction of the three-dimensional direction of individual proton tracks based on two projections, as illustrated in Figure 2.11. Using these projections, we apply the Hough transform followed by moment analysis to determine the correct direction of the track, denoted as θ_p, for each projection.

Let $\theta_p^{(xz)}$ and $\theta_p^{(xy)}$ denote the two directions reconstructed from the (xz) and (xy) projections, respectively. Furthermore, we define $\ell_{(xz)}$ and $\ell_{(xy)}$ as the track lengths in each respective projection. Since the quantities $\ell_{(xz)} \cos\theta_p^{(xz)}$ and $\ell_{(xy)} \cos\theta_p^{(xy)}$ both represent the projection of the track along the x-axis, they should be averaged to obtain a more accurate estimate of the proton track x-component. Therefore, the 3D track vector, with a magnitude corresponding to the proton *range*, can be written as:

$$\vec{r} = \left(\frac{\ell_{(xz)} \cos\theta_p^{(xz)} + \ell_{(xy)} \cos\theta_p^{(xy)}}{2}, \ell_{(xy)} \sin\theta_p^{(xy)}, \ell_{(xz)} \sin\theta_p^{(xz)} \right), \quad \hat{r}_{reco} = \frac{\vec{r}}{\|\vec{r}\|}. \quad (4.1.1)$$

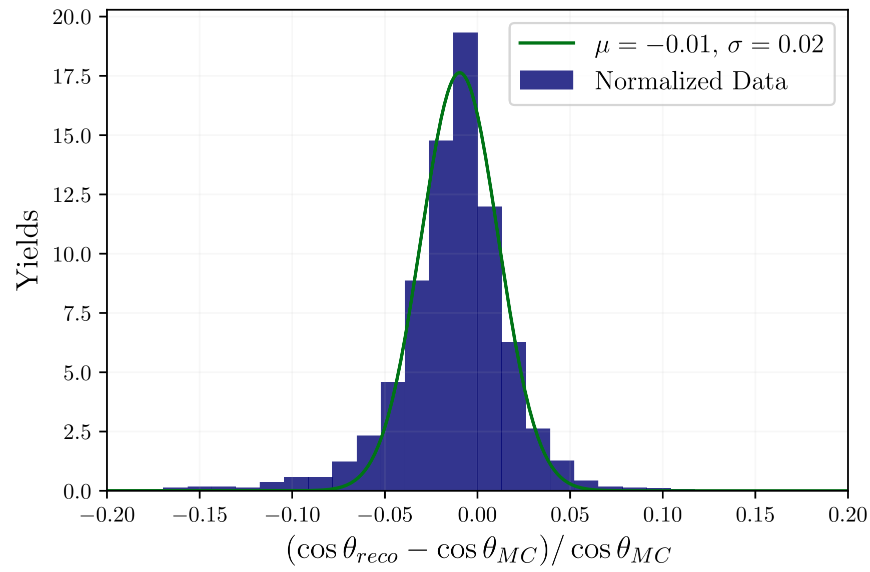

FIGURE 4.1: *Normalized residuals between the reconstructed cosine of the angle* $\cos\theta_{reco}$ *and the Monte Carlo truth* $\cos\theta_{MC}$ *are presented; see the text for details.*

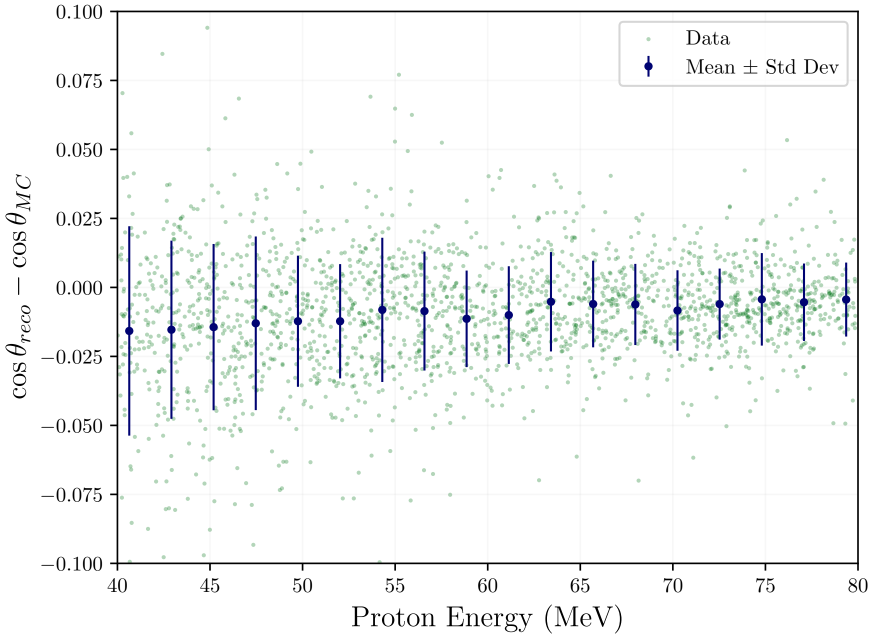

FIGURE 4.2: *Residuals between the reconstructed and true proton angles as a function of proton energy are shown. The blue error bars represent the residuals within a constant energy bin.*

Now that we know the neutron source is aligned with the x-axis (as explained in

Section 2.3), we can start to extract a crucial piece of information needed to reconstruct the neutron energy: the cosine of the angle between the incoming neutron direction and the outgoing proton direction after scattering (see Figure 1.7). This can be calculated as follows:

$$\hat{r}_{reco} \cdot \hat{x} = \cos\theta_{reco}. \tag{4.1.2}$$

To validate these results, we compared them with the Monte Carlo truth. As shown in Figure 4.1, the relative difference between $(\cos\theta_{reco} - \cos\theta_{MC})/\cos\theta_{MC}$ reveals a 2% precision in the determination of the cosine of the angle. Additionally, Figure 4.2 displays the residuals as a function of the proton energy, indicating no clear dependence of the residuals on the proton energy.

4.1.2 From ranges to proton energies

In Section 3.2.2, we described a straightforward method for estimating track lengths using the projection on the sensor. This simple approach was applied after correcting for aberrations and noise in the image. Since the range of a proton in the scintillator corresponds to the full three-dimensional track length, we can evaluate the proton range using:

$$R_{reco} = \sqrt{\left(\frac{\ell_x^{(xz)} + \ell_x^{(xy)}}{2}\right)^2 + \left(\ell_y^{(xy)}\right)^2 + \left(\ell_z^{(xz)}\right)^2}, \tag{4.1.3}$$

where $\ell_x^{(xz)}$ and $\ell_x^{(xy)}$ represent the track projections along the x-axis in the (xz) and (xy) planes, respectively. Since these projections correspond to the same physical quantity, they are averaged for a more accurate estimate. Similarly, $\ell_y^{(xy)}$ and $\ell_z^{(xz)}$ refer to the track lengths projected along the y-axis in the (xy) plane and the z-axis in the (xz) plane, respectively. This formulation provides the total 3D track length, or *range*, of the proton.

To validate the results obtained using this reconstruction method, the reconstructed ranges were compared with the Monte Carlo truth. In Figure 4.3, the relative differences $(R_{reco} - R_{MC})/R_{MC}$ are shown, demonstrating a precision of approximately 5% in the range reconstruction. This percentage was derived from a Gaussian fit applied to the normalized yield distribution. However, it is evident that the chosen Gaussian model does not fully account for the tails observed in the distribution, leading to an asymmetry. Furthermore, in Figure 4.4, the residuals as a function of proton energy do not show any clear energy dependence.

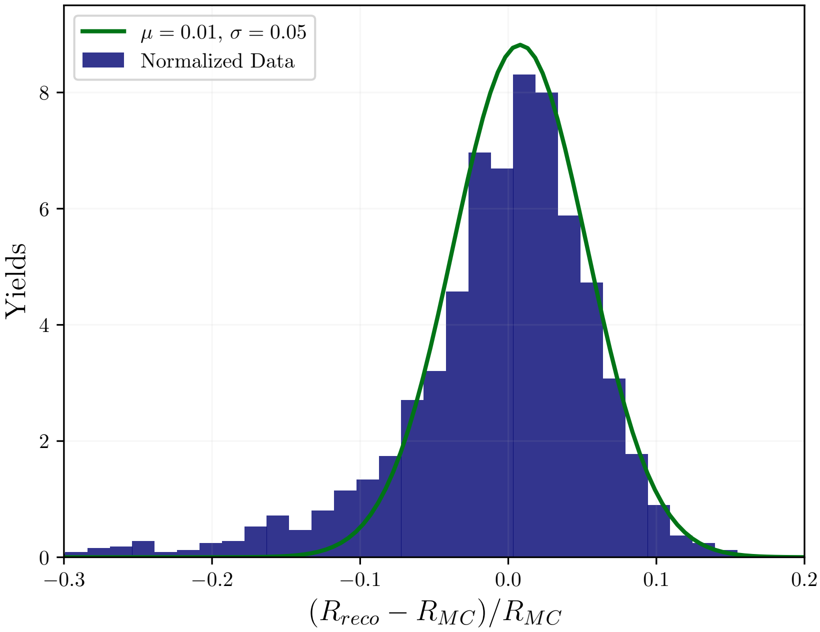

FIGURE 4.3: *Normalized residuals between the reconstructed proton ranges* (R_{reco}) *and Monte Carlo truth* (R_{MC}).

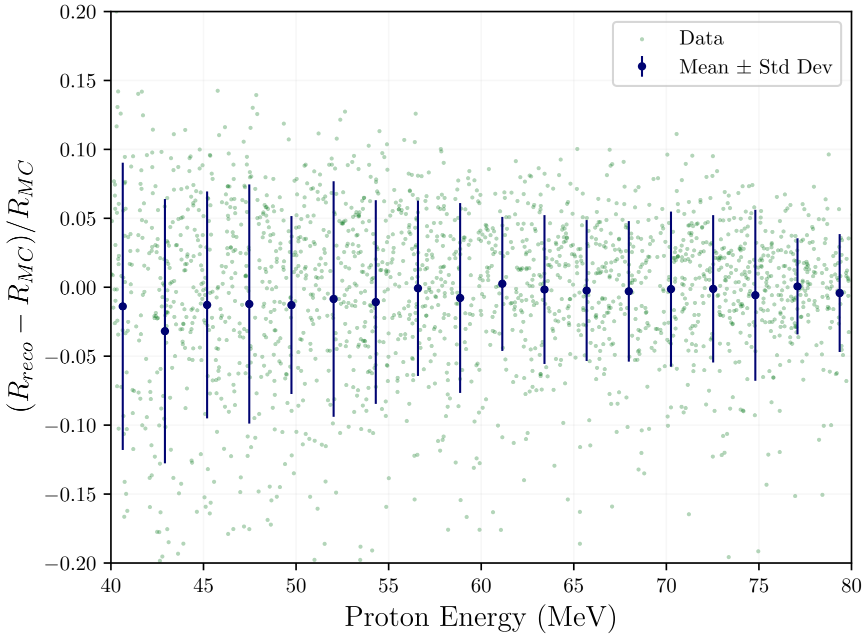

FIGURE 4.4: *Residuals between the reconstructed and true proton ranges as a function of proton energy. Blue error bars represent the residuals within a constant energy bin.*

A well-defined correlation exists between the proton energy and its range, as described in Equation 1.2.2. This relationship plays a crucial role in the neutron energy determination, in fact by inverting the equation, the proton energy can be calculated from the measured track length, i.e. its range. The proton kinetic energy is the second key piece of information required to evaluate the incident neutron energy, as described in Equation 1.2.1.

To establish a precise relationship between the range and proton energy, a new Monte Carlo dataset was specifically generated, covering the entire spectrum of proton energies relevant to fast neutron scattering. This dataset was then used to perform a two-parameter fit, yielding an accurate empirical law that links the proton range to its energy (see Figure 4.5). The fitted parameters result:

$$\alpha = (1.867 \pm 0.013) \cdot 10^{-2}\ \text{mm/MeV}, \quad p = (1.803 \pm 0.002). \tag{4.1.4}$$

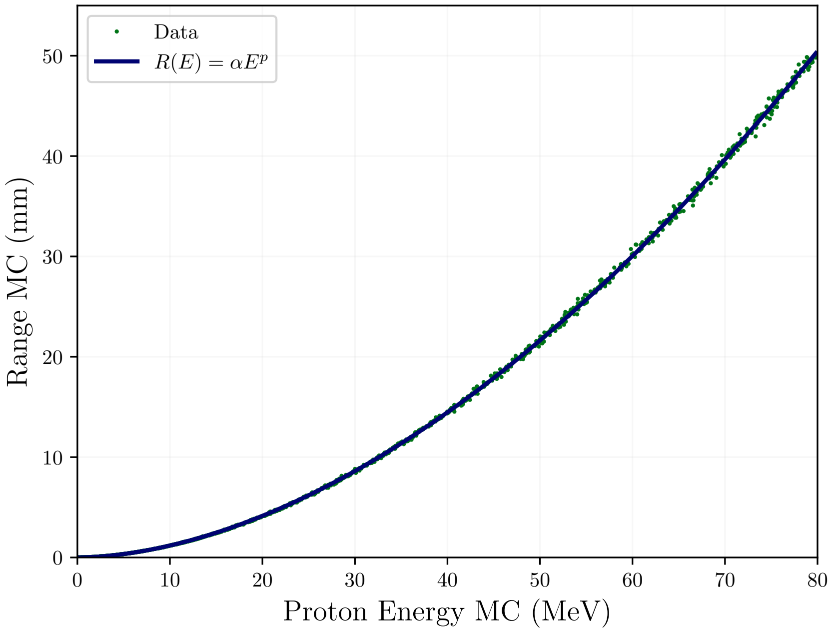

FIGURE 4.5: *Relationship between range and proton energy. A two-parameter fit is performed to determine an empirical law that links proton range to its energy.*

4.1.3 Neutron energy

In order to reconstruct the energy of monoenergetic neutrons undergoing single scattering with protons in the scintillator, we can use the results obtained in Section 4.1.1 and

Section 4.1.2. The relation we use for this purpose is given in Equation 1.2.1, which links the reconstructed proton track direction, orientation, and energy to the incident neutron energy. Figure 4.6 shows the normalized residuals between the reconstructed and true neutron energies, indicating a precision of 5% in the energy reconstruction. This precision was estimated by fitting a Gaussian model to the normalized data presented in the figure.

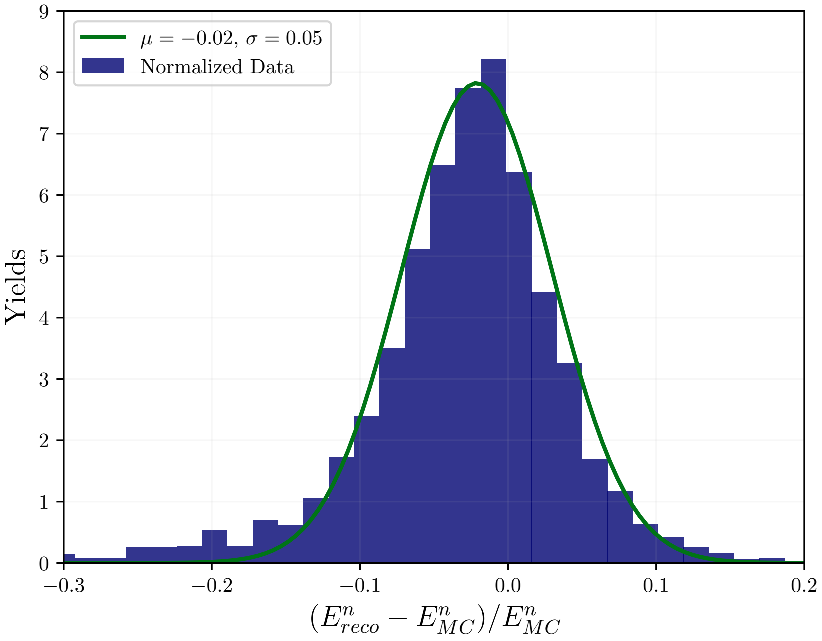

FIGURE 4.6: *Normalized residuals between reconstructed and true neutron energy.*

4.2 Double scattering reconstruction

In this section, we explain how the neutron energy reconstruction procedure can be generalized to double scattering events. What follows is an overview of an analysis that will be systematically carried out in the near future.

4.2.1 Tracks matching

The first step in studying double scattering events, as illustrated in Figure 4.7, is to segment the tracks so they can be treated as two independent single-scattering cases. This approach allows us to apply all the techniques previously developed for single scattering twice, once for each track segment.

To achieve this, it is essential to determine which pixels belong to each track. For this purpose, a clustering algorithm called *K-means* [16] was employed. This algorithm effectively partitions the pixels into distinct clusters, corresponding to individual tracks. By referencing both projections, we obtain clustering results that can, however, lead to four possible 3D reconstructions. This ambiguity arises because each track in one projection can be paired with either of the tracks in the other projection, resulting in four possible combinations of track pairings. These combinations need to be resolved to identify the correct 3D configuration. To pair the tracks, we take advantage of the fact that the two projections share the same x-axis. By comparing the x-coordinate ranges of the tracks in each projection, we match the tracks whose x intervals are most similar. This approach allows us to assign tracks from one projection to the corresponding tracks in the other, resolving the ambiguity.

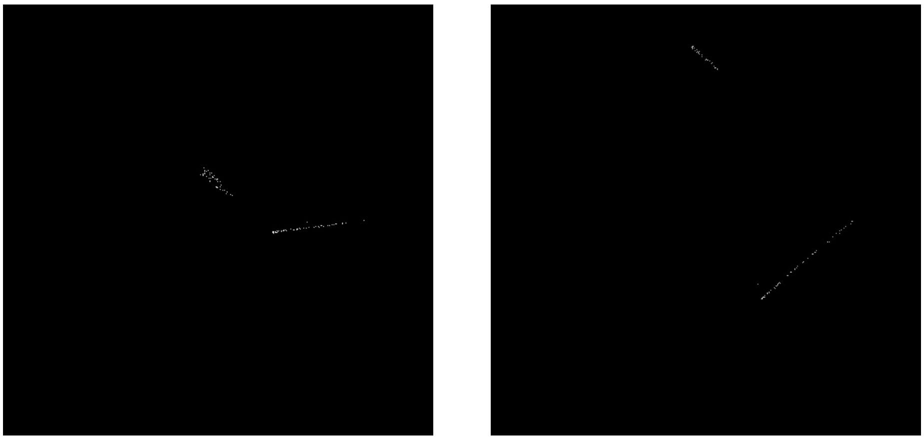

(A) (xz) *projection.*

(B) (xy) *projection.*

FIGURE 4.7: *Projections of a double-scattering event on the sensor.*

In this way, we have reduced the problem of double scattering to analyzing two single scattering events using the techniques introduced in Chapter 3.

4.2.2 Neutron energy from track endpoints

The second step in double scattering event analysis is to reconstruct the scattering topology using the information provided by the reconstruction techniques introduced in this work. Once the energies of the double scattering events in the decoupled projections are reconstructed, the next step is to combine the information. Referring to the sketch in Figure 1.8, we proceed gradually: first, we must connect the endpoints of each track in such a way that we can determine the direction θ_{p_2} of the first proton to be analyzed. By applying Equation 1.2.1, we can then determine the neutron energy ($E_n^{(2)}$ in the scheme) from the previous step. After this, by exploiting the fact that the scattering angle between the outgoing proton and neutron forms a 90° angle, we can determine the second direction θ_{p_1}. Finally, by applying Equation 1.2.1 once again, we arrive at the calculation of the initial neutron energy.

Conclusion and future developments

The primary goal of this thesis is to investigate and develop novel imaging techniques that could contribute to advancements in neutron detectors like RIPTIDE, which aims to track fast neutrons by visualizing the scintillation of proton recoil tracks. This research devises a track reconstruction method based on stereoscopic imaging. This method employs two orthogonal projections of proton-recoil tracks reaching the sensor, obtained from Monte Carlo simulations.

Imaging methods have proven to be effective for reconstructing particle tracks with high accuracy. This technique yields promising results regarding reconstructing the direction and orientation of proton recoil tracks in 3D. Integrated with deep learning algorithms for optical aberration correction, it significantly enhances the precision of track length estimation. As a result, the proposed method shows substantial potential for neutron energy and kinematics reconstruction within the RIPTIDE project. It is important to note that these techniques could be generalized and scaled to meet the needs of other experiments that use scintillation light analysis to reconstruct decay topologies.

The aim of this study is to demonstrate the viability of the proposed method. Therefore, the analysis is limited to a representative case. In fact, the dataset used in this study consists of monoenergetic neutrons at 100 MeV, which result in single and double scattering events with protons emerging at energies greater than 40 MeV. This restricts the range of proton energies considered in the analysis. A more comprehensive study should include protons with energies down to at least 20 MeV, as protons below this threshold are more difficult to distinguish due to reduced track visibility. Extending the analysis to lower-energy protons would provide a more robust evaluation of the system's performance across a wider range of neutron energies. Additionally, the dataset of neutron events should be expanded in terms of the number of events to ensure better statistical significance and to provide a larger training dataset for the deep learning methods used in track reconstruction.

Furthermore, the photon propagation codes from the scintillator to the sensor are approximate, especially regarding the simulation of lenses and the image intensifier. To achieve image reproduction that closely resembles reality, the optical system should be simulated with greater precision. This includes exploring configurations that minimize optical aberrations and maximize the depth of field, ensuring the best possible imaging performance for our system.

The project is still in its early stages and requires significant further work, both in terms of constructing the experimental setup and refining the Monte Carlo simulations. The first priority will be to continue and systematize the analysis of double scattering events, which is only briefly explored in this work. Following that, it will be crucial to classify the dataset to select only the events of interest and to distinguish them from the charged particles that constitute the background. To achieve this, several approaches are being considered, including the use of deep learning techniques for event classification. This approach would enable the entire analysis to be fully automated, greatly improving efficiency and accuracy. Applying these advanced methods will enhance the identification of relevant neutron scattering events, further advancing the system's precision and scalability in neutron detection and analysis.

Bibliography

[1] S. Agostinelli et al. “Geant4—a simulation toolkit”. In: *Nuclear Instruments and Methods in Physics Research Section A: Accelerators, Spectrometers, Detectors and Associated Equipment* 506.3 (2003), pp. 250–303. DOI: `10.1016/S0168-9002(03)01368-8`.

[2] G. Battistoni et al. “Measuring the Impact of Nuclear Interaction in Particle Therapy and in Radio Protection in Space: the FOOT Experiment”. In: *Frontiers in Physics* 8 (2021). DOI: `10.3389/fphy.2020.568242`.

[3] U. Bravar et al. “Atmospheric neutron measurements with the SONTRAC science model”. In: *IEEE Nuclear Science Symposium Conference Record, 2005* 2 (2005), pp. 634–638. DOI: `10.1109/NSSMIC.2005.1596340`.

[4] D.A. Brown et al. “ENDF/B-VIII.0: The 8th Major Release of the Nuclear Reaction Data Library with CIELO-project Cross Sections, New Standards and Thermal Scattering Data”. In: *Nuclear Data Sheets* 148 (2018), pp. 1–142. DOI: `10.1016/j.nds.2018.02.001`.

[5] Rene Brun et al. *root-project/root: v6.18/02.* Version v6-18-02. June 2020. DOI: `10.5281/zenodo.3895860`.

[6] J. Chadwick. “The Existence of a Neutron”. In: *Proceedings of the Royal Society of London. Series A, Containing Papers of a Mathematical and Physical Character* 136.830 (1932), pp. 692–708. DOI: `http://www.jstor.org/stable/95816`.

[7] François Chollet et al. *Keras*. `https://keras.io`. 2015.

[8] L. I. Dorman. *Solar Neutrons and Related Phenomena*. Springer, 2010.

[9] Richard O Duda and Peter E Hart. “Use of the Hough transformation to detect lines and curves in pictures”. In: *Communications of the ACM* 15.1 (1972), pp. 11–15. DOI: `10.1145%2F361237.361242`.

[10] C. Guerrero et al. “Performance of the neutron time-of-flight facility n_TOF at CERN”. In: *The European Physical Journal A* 49.2 (2013), p. 27. DOI: `10.1140/epja/i2013-13027-6`.

[11] Chenyao Han et al. “A background suppression detector array for fast neutron measurement in space science study”. In: *Measurement* 230 (2024), p. 114479. DOI: `10.1016/j.measurement.2024.114479`.

[12] D. M. Hassler et al. “Mars’ Surface Radiation Environment Measured with the Mars Science Laboratory’s Curiosity Rover”. In: *Science* 343.6169 (2014), p. 1244797. DOI: `10.1126/science.1244797`.

[13] Kaiming He et al. “Deep Residual Learning for Image Recognition”. In: *2016 IEEE Conference on Computer Vision and Pattern Recognition (CVPR)* (2015), pp. 770–778.

[14] Sepp Hochreiter. “The Vanishing Gradient Problem During Learning Recurrent Neural Nets and Problem Solutions”. In: *International Journal of Uncertainty, Fuzziness and Knowledge-Based Systems* 6 (Apr. 1998), pp. 107–116. DOI: `10.1142/S0218488598000094`.

[15] Yann LeCun, Yoshua Bengio, and Geoffrey Hinton. “Deep learning”. In: *Nature* 521.7553 (2015), pp. 436–444. DOI: `10.1038/nature14539`.

[16] S. Lloyd. “Least squares quantization in PCM”. In: *IEEE Transactions on Information Theory* 28.2 (1982), pp. 129–137. DOI: `10.1109/TIT.1982.1056489`.

[17] C. Massimi, A. Musumarra, and N. Patronis. *Measurement of the neutron-neutron scattering length at the CERN n_TOF facility.* Tech. rep. Geneva: CERN, 2020. DOI: `https://cds.cern.ch/record/2730967`.

[18] John W. Norbury. “Nuclear physics and space radiation”. In: *J. Phys. Conf. Ser.* 381 (2012). Ed. by Sean Freeman et al., p. 012117. DOI: `10.1088/1742-6596/381/1/012117`.

[19] C. Pisanti et al. “Riptide: a proton-recoil track imaging detector for fast neutrons”. In: *Journal of Instrumentation* 19.02 (Feb. 2024), p. C02074. DOI: `10.1088/1748-0221/19/02/C02074`.

[20] Olaf Ronneberger, Philipp Fischer, and Thomas Brox. "U-Net: Convolutional Networks for Biomedical Image Segmentation". In: *International Conference on Medical image computing and computer-assisted intervention*. Springer. 2015, pp. 234–241. DOI: 10.1007/978-3-319-24574-4_28.

[21] J.M. Ryan et al. "A scintillating plastic fiber tracking detector for neutron and proton imaging and spectroscopy". In: *Nuclear Science Symposium* (1999). DOI: 10.1109/NSSMIC.1999.842532.

[22] National Institute of Standards and Technology. *Security Requirements for Cryptographic Modules*. Tech. rep. Federal Information Processing Standards Publications (FIPS PUBS) 140-2, Change Notice 2 December 03, 2002. Washington, D.C.: U.S. Department of Commerce, 2001. DOI: 10.6028/nist.fips.140-2.

[23] Eljen Technology. *General Purpose EJ-200, EJ-204, EJ-208, EJ-212, available online at https://eljentechnology.com/products/plastic-scintillators/ej-200-ej-204-ej-208-ej-212*.

[24] S.M. Valle et al. "The MONDO project: A secondary neutron tracker detector for particle therapy". In: *Nuclear Instruments and Methods in Physics Research Section A: Accelerators, Spectrometers, Detectors and Associated Equipment* 845 (2017), pp. 556–559. DOI: 10.1016/j.nima.2016.05.001.

[25] M. Visvalingam and J. D. Tandy. "The neutron method for measuring soil moisture content - a review". In: *Journal of soil science* 23 (1972), pp. 499–511. DOI: 10.1111/j.1365-2389.1972.tb01680.x.